Article

Historical Attributions and Future Projections of Gross Primary Productivity in the Yangtze River Basin under Climate Change Based on a Novel Coupled LUE-RE Model

Hong Du [1], Jian Wu [2,3], Sidong Zeng [1,2,3,*] and Jun Xia [2,4]

1   College of Resources and Environmental Science, South-Central Minzu University, Wuhan 430074, China; duhong@scuec.edu.cn
2   Chongqing Institute of Green and Intelligent Technology, Chinese Academy of Sciences, Chongqing 400714, China; wujian@cigit.ac.cn (J.W.)
3   Chongqing School, University of Chinese Academy of Sciences, Chongqing 400714, China
4   State Key Laboratory of Water Resources and Hydropower Engineering Science, Wuhan University, Wuhan 430072, China
*   Correspondence: zengsidong@cigit.ac.cn

Abstract: Attributions and predictions of gross primary productivity (GPP) under climate change is of great significance for facilitating a deeper understanding of the global and regional terrestrial carbon cycle and assessing ecosystem health. In this study, we have designed a novel approach to simulate GPP based on the satellite and meteorological data compiling the advantages of the light use efficiency model with regression methods (LUE-RE model), which overcomes the limitation of the satellite-based method in GPP simulation and projection in the future time without satellite data. Based on the proposed method, results show that GPP in the Yangtze River Basin shows a significant increase trend in the historical period. Elevated CO_2 dominates the changes of GPP in the Yangtze River Basin. In the future, with the increase in elevated CO_2 and climate change, the trend of GPP growth is more obvious. The growth slopes under different scenarios are 2.65 $gCm^{-2}year^{-1}a^{-1}$, 12.34 $gCm^{-2}year^{-1}a^{-1}$, 24.91 $gCm^{-2}year^{-1}a^{-1}$, and 39.62 $gCm^{-2}year^{-1}a^{-1}$. There are obvious seasonal differences in the future changes of GPP in the Yangtze River Basin, of which the GPP changes mostly in spring. The spatial patterns show that higher GPP is concentrated in the upper stream, while the low values are mainly concentrated in the middle reaches. This study contributes a new method to project GPP and highlights that stakeholders should pay more attention to the significant GPP increases in spring in the future.

Keywords: gross primary productivity; LUE-RE model; attribution analysis; future projection

1. Introduction

As the main component of the terrestrial ecosystem, vegetation is an important link in the exchange of energy, water, and carbon between land surface and atmosphere [1,2]. Gross primary productivity (GPP), the total amount of carbon absorbed by vegetation at ecosystem scale [3], directly reflects the productivity of vegetation under specific environmental conditions, indicating the growth characteristics and health status of terrestrial ecosystems [4]. Moreover, GPP is the main component of terrestrial carbon sequestration and plays a key role in the global carbon balance, providing the terrestrial ecosystem with the ability to partially offset anthropogenic CO_2 emissions [5]. Accurate estimation and attribution of GPP is of great significance for facilitating a deeper understanding of the global and regional terrestrial carbon cycle and assessing ecosystem health [6]. In addition, future climate changes will inevitably affect the global vegetation dynamics, so it is extremely important to project the possible changes in vegetation productivity under future climate changes [7].

So far, there is still no technology available to measure GPP directly, because of the lack of measuring at scales greater than the leaf level [8]. At ecosystem scale, the eddy covariance (EC) technique, which quantifies the continuous net ecosystem exchange (NEE) of CO_2, can be used to infer GPP by separating ecosystem respiration and GPP from NEE [9]. However, this method limits the estimate of GPP from tens of meters to several kilometers, making it difficult to calculate at a large scale [10,11]. In order to estimate and project GPP at regional and global scales, ecosystem models have been developed and applied as scientific tools to obtain GPP [12]. This mainly includes process-based models and LUE models [13,14]. The process-based models consider the growth processes of vegetation, such as photosynthesis, respiration, and evapotranspiration. Although this provides a solid physiological and ecological mechanism for the models, it also leads to a complex simulation process, which is easily limited by a large number of model inputs and physical parameters. Moreover, the parameters vary greatly between different regions and vegetation, thereby increasing the difficulties of obtaining appropriate parameters, subsequently leading to more difficulties in GPP estimation.

The LUE models are generally based on the theory of light use efficiency, stating a relatively constant relationship exists between photosynthetic carbon uptake and absorbed photosynthetically active radiation at the canopy level [15,16]. Potter et al. [17] developed the first CASA model for estimating global vegetation productivity, and then a series of LUE models have been developed, including the GLO-PEM model [18], MOD17 GPP model [19], Vegetation Photosynthesis Model [20], Eddy Covariance Light Use Efficiency Model [21], etc. In contrast to the process-based models which are limited by a large number of model inputs and physical parameters, LUE models have less model inputs and could simulate GPP at high spatial–temporal resolution by means of high-resolution remote sensing products [22,23]. As a consequence, LUE models are widely used in current research. In addition, LUE models directly use a wide range of satellite remote sensing data; they have great potential to fully solve the dynamic changes of GPP in time and space. At present, a lot of researchers have also proven that the LUE models are effective tools for large-scale research of GPP [24–26]. Moreover, the LUE model has been improved in different degrees during its development, treating the fraction of photosynthetic active radiation in disparate ways or using more reasonable means to represent temperature stress (TS) and water stress (WS) [27]. Despite these advantages, it is precisely because they directly use satellite data that are only available in history, which makes it difficult to predict GPP in the future, and there are few studies applying LUE models to future GPP predictions [28]. In order to investigate the possible changes in GPP in the future using the LUE model, maintaining the advantages of the LUE model within fewer parameters, further improvements are still needed in the LUE model to facilitate its application in GPP predictions under future climate change.

In this study, in order to analyze the effects of climate change on historical GPP and predict the possible changes in future GPP in the Yangtze River Basin under climate change, a new method for simulating and predicting GPP by coupling the LUE model and regression model is proposed, and then the proposed model is used to attribute and project the GPP changes in the Yangtze River Basin. The main objectives of this study are as follows: (1) to develop a new LUE-RE method for GPP simulation and projection and validate its performances, (2) to investigate the spatial–temporal changes of historical GPP and quantifying the contributions of different climate factors on historical GPP changes, and (3) to project the future GPP changes under different climate change scenarios based on Coupled Model Intercomparison Project Phase 6 (CMIP6) in the Yangtze River Basin.

2. Study Area and Dataset

2.1. Study Area

The Yangtze River Basin is located between 24° to 35°N and 90° to 122°E within a total area of over 1.8 million km^2, accounting for 18.8% of China's land area (Figure 1). The Yangtze River has a total length of 6300 km, flows through 11 provinces and cities

such as Qinghai, Tibet, Sichuan, Chongqing, and Yunnan, while the tributaries extend to eight provinces (autonomous regions) such as Guizhou, Gansu, Shaanxi, Henan, Zhejiang, Guangxi, Guangdong, and Fujian. The upper reaches of the Yangtze River originate from above Yichang, with a watershed area of 1 million km^2. The middle reaches from Yichang to Hukou, with a drainage area of 680,000 km^2. Downstream from below the Hukou lake mouth, the watershed area is 120,000 km^2. As a unique and complete natural ecosystem, the Yangtze River Basin has powerful functions such as soil and water conservation, biological breeding, oxygen and carbon release, environmental purification, etc. It plays an important role in maintaining the ecological balance and security of surrounding areas and even the whole country.
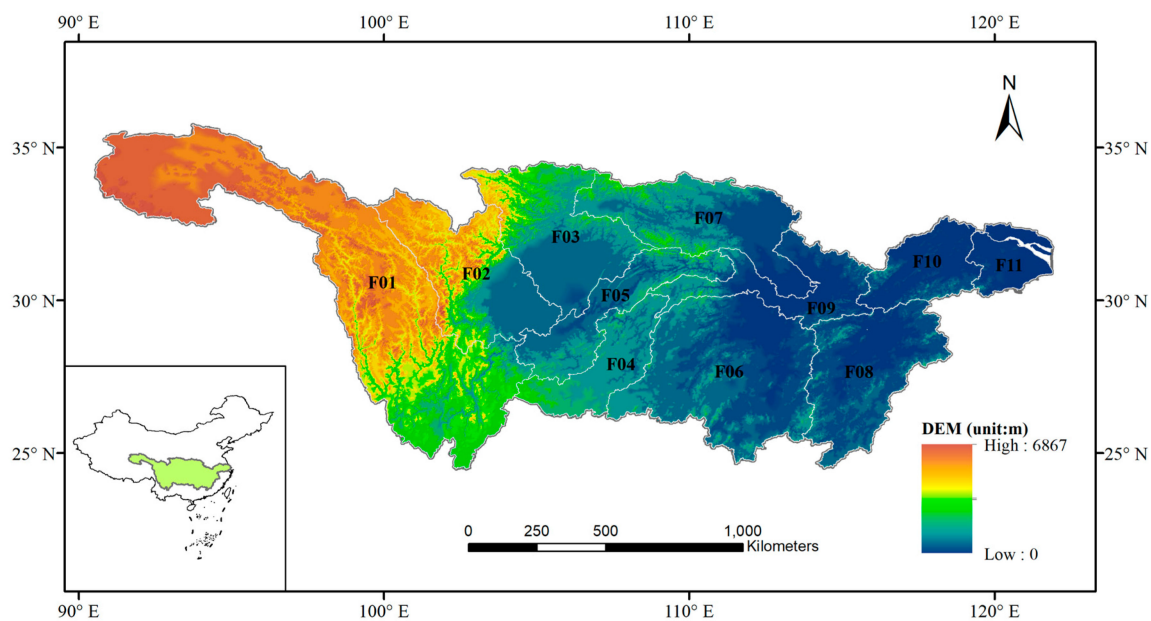

Figure 1. Overview of the Yangtze River Basin, including 11 sub basins (F01: Jinsha River, F02: Mintuo River, F03: Jialing River, F04: Wujiang River, F05: Upper trunk stream, F06: Dongting Lake, F07: Hanjiang River, F08: Poyang Lake, F09: Middle trunk stream, F10: Lower trunk stream, F11: Taihu Lake).

2.2. Dataset

The GPP dataset based on the LUE model by improving the optimal temperature for vegetation growth was used in this study, which could be calculated by Equation (1). The spatial resolution of these data is 0.05°, and the time range is from 2001 to 2018. The resampling method is used to adjust the spatial resolution to 0.1°. This dataset has been validated within R^2 and RMSE of 0.73~0.76 and 40 $gCm^{-2}mon^{-1}$ (1.3 $gCm^{-2}d^{-1}$), indicating a better simulation accuracy [29].

$$GPP = PAR \times FPAR \times \varepsilon_{max} \times \frac{1.1814 \times (1 + e^{0.3 \times (-T_{opt} - 10 + T_{air})})}{1 + e^{0.2 \times (T_{opt} - 10 - T_{air})}} \times (0.25 + 0.75 \times \frac{ET}{RN}) \quad (1)$$

where *PAR* is photosynthetically active radiation; *FPAR* is fraction of photosynthetically active radiation; ε_{max} is efficiency of light energy conversion under ideal conditions; T_{opt} is the optimum temperature for vegetation growth; *ET* is the actual evapotranspiration; *RN* is surface net radiation.

In addition, the meteorological data including temperature, precipitation, vapor pressure deficit, and short-wave radiation used in this study were obtained from the China Meteorological Forcing Dataset, which is developed by the Institute of Tibetan Plateau Research, Chinese Academy of Sciences [30]. The time range used is from January 2001 to December 2018 with the spatial resolution 0.1°. The historical CO_2 concentration data were

also obtained from the Wariguan Global Atmospheric Background Station, Global Monitoring Laboratory, National Oceanic and Atmospheric Administration (NOAA), Hainan Prefecture, Qinghai Province, China. It is the only atmospheric background observation station in the Northern Hemisphere, and its observation results can represent the atmospheric greenhouse gas concentration and its changes in the middle latitudes of the Northern Hemisphere. The land use data used are obtained from European Space Agency CCI-LC products (https://www.esa-landcover-cci.org/, accessed on 1 September 2023).

To predict the future GPP in the Yangtze River Basin, the projected future climate data including daily precipitation, temperature, relative humidity, and radiation data are obtained from the selected GCMs under four Shared Socioeconomic Pathways (SSP) scenarios including SSP1-2.6, SSP2-4.5, SSP3-7.0, and SSP5-8.5 from Coupled Model Intercomparison Project Phase 6 (CMIP6). Meanwhile, the future elevated CO_2 data are from the National Data Center for Ecological Sciences [31]. This dataset is based on historical fossil fuel CO_2 emissions and monthly average CO_2 concentration data. For the average CO_2 concentration under the SSP-RCPs scenario from 2015 to 2150, based on the historical spatial distribution of CO_2 concentration, the monthly spatial distribution data of CO_2 concentration in the next 2015–2150 years under different scenarios were obtained.

3. Methodology

3.1. Research Framework

The research framework is shown in Figure 2. Firstly, the LUE-RE GPP model is constructed based on the multivariate linear regression method using the LUE GPP and historical climate variables including CO_2, temperature (TEMP), precipitation (PREC), solar radiation (SRAD), etc. in each unit considering the land use type classified into forest, grass, shrub, and crop. Based on the LUE-RE GPP model, the spatial–temporal variation of the historical GPP is investigated and then the sensitivities of GPP to the climate variables and the attribution of GPP are conducted. After that, the future GPP is projected under different SSP scenarios based on CMIP6 climate model and the LUE-RE GPP model.
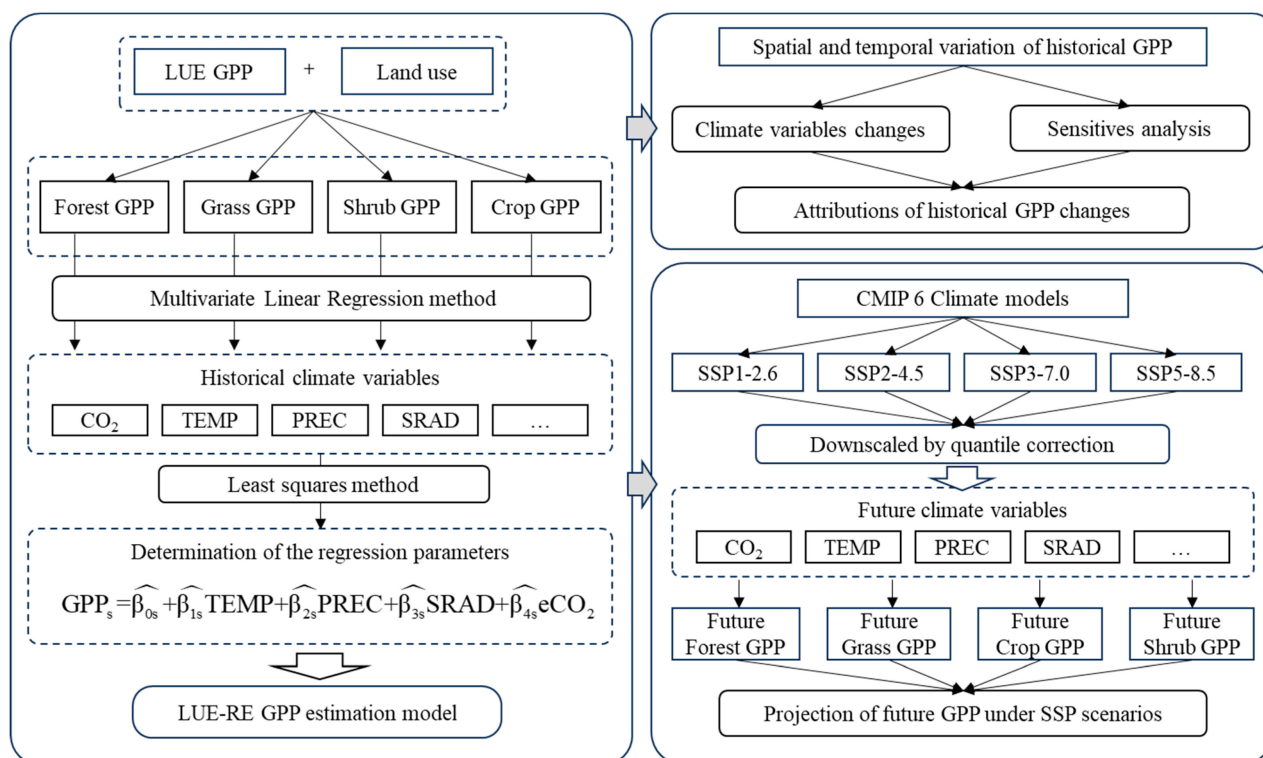

Figure 2. Framework of this study.

3.2. The LUE-RE GPP Model

Firstly, the LUE GPP values in each unit are divided into forest GPP, grassland GPP, crop GPP, and shrub GPP based on the vegetation type. For example, the LUE GPP is separated into different types of GPP according to the land use datasets.

$$GPP = GPP_1 + GPP_2 + GPP_3 + GPP_4 \tag{2}$$

where GPP_1, GPP_2, GPP_3, and GPP_4 represent forest GPP, grassland GPP, crop GPP, and shrub GPP, respectively.

On the pixel scale, a multivariate linear regression model between GPP_s and each factor of a vegetation is set up as follows:

$$GPP_s = \beta_{0s} + \beta_{1s}TEMP + \beta_{2s}PREC + \beta_{3s}SRAD + \beta_{4s}eCO_2 + \varepsilon_s \tag{3}$$

where $\beta_{0s}, \beta_{1s}, \beta_{2s}, \beta_{3s}, \beta_{4s}$ are parameters for the response of the gross primary productivity of the s vegetation type to temperature, precipitation, solar radiation, vapor pressure deficit, and elevated CO_2, respectively. ε_s is an unobservable random variable with a mean of zero and a variance of $\sigma^2 > 0$, which is called the Error term and is usually assumed $\varepsilon \sim N(0, \sigma^2)$. If a total of n years of time series data have been obtained in the existing years of history, there are:

$$\begin{cases} GPP_{s1} = \beta_{0s} + \beta_{1s}TEMP_1 + \beta_{2s}PREC_1 + \beta_{3s}SRAD_1 + \beta_{4s}eCO_{21} + \varepsilon_{s1} \\ GPP_{s2} = \beta_{0s} + \beta_{1s}TEMP_2 + \beta_{2s}PREC_2 + \beta_{3s}SRAD_2 + \beta_{4s}eCO_{22} + \varepsilon_{s2} \\ \qquad\qquad\qquad\qquad \vdots \\ GPP_{sn} = \beta_{0s} + \beta_{1s}TEMP_n + \beta_{2s}PREC_n + \beta_{3s}SRAD_n + \beta_{4s}eCO_{2n} + \varepsilon_{sn} \end{cases} \tag{4}$$

$$Y_s = \begin{bmatrix} GPP_{s1} \\ GPP_{s2} \\ \vdots \\ GPP_{sn} \end{bmatrix}, \ \beta_s = \begin{bmatrix} \beta_{0s} \\ \beta_{1s} \\ \vdots \\ \beta_{4s} \end{bmatrix}, \ \varepsilon_s = \begin{bmatrix} \varepsilon_{s1} \\ \varepsilon_{s2} \\ \vdots \\ \varepsilon_{sn} \end{bmatrix} \tag{5}$$

$$X = \begin{bmatrix} 1 & TEMP_1 & PREC_1 & SRAD_1 & eCO_{21} \\ 1 & TEMP_2 & PREC_2 & SRAD_2 & eCO_{22} \\ 1 & \vdots & \vdots & \vdots & \vdots \\ 1 & TEMP_n & PREC_n & SRAD_n & eCO_{2n} \end{bmatrix} \tag{6}$$

The above formula is expressed as matrix representation:

$$\begin{cases} Y_s = X\beta_s + \varepsilon_s \\ \varepsilon_s \sim N(1, \sigma^2 In) \end{cases} \tag{7}$$

Using the least squares method to calculate the estimated values of regression parameters, by minimizing the sum of squares of errors and seeking the best functional match of the data, the optimal estimation value of the regression parameters is obtained to minimize the sum of squares of deviations:

$$Q(\widehat{\beta_s}) = \sum_{i=1}^{n} (GPP_{si} - \widehat{\beta_{0s}} - \widehat{\beta_{1s}}TEMP_i - \widehat{\beta_{2s}}PREC_i - \widehat{\beta_{3s}}SRAD_i - \widehat{\beta_{4s}}eCO_{2i})^2 \tag{8}$$

According to the principle of extreme value in calculus, $\widehat{\beta}$ should meet the following equations:

$$
\begin{cases}
\left.\dfrac{\partial Q}{\partial \widehat{\beta_{0s}}}\right|_{\beta_{0s}=\widehat{\beta_{0s}}} = -2\sum_{i=1}^{n}\left(GPP_{si}-\widehat{GPP_{si}}\right)=0 \\[2mm]
\left.\dfrac{\partial Q}{\partial \widehat{\beta_{1s}}}\right|_{\beta_{1s}=\widehat{\beta_{1s}}} = -2\sum_{i=1}^{n}\left(GPP_{si}-\widehat{GPP_{si}}\right)TEMP_i=0 \\[2mm]
\left.\dfrac{\partial Q}{\partial \widehat{\beta_{2s}}}\right|_{\beta_{2s}=\widehat{\beta_{2s}}} = -2\sum_{i=1}^{n}\left(GPP_{si}-\widehat{GPP_{si}}\right)PREC_i=0 \\[2mm]
\left.\dfrac{\partial Q}{\partial \widehat{\beta_{3s}}}\right|_{\beta_{ss}=\widehat{\beta_{ss}}} = -2\sum_{i=1}^{n}\left(GPP_{si}-\widehat{GPP_{si}}\right)SRAD_i=0 \\[2mm]
\left.\dfrac{\partial Q}{\partial \widehat{\beta_{4s}}}\right|_{\beta_{4s}=\widehat{\beta_{4s}}} = -2\sum_{i=1}^{n}\left(GPP_{si}-\widehat{GPP_{si}}\right)eCO_{2i}=0
\end{cases}
\tag{9}
$$

When $(X'X)^{-1}$ present, the least squares estimate of the regression parameters is as follows:

$$
\widehat{\beta_s} = (X'X)^{-1}X'Y_s
\tag{10}
$$

The final model for the gross primary productivity of vegetation is as follows:

$$
GPP_s = \widehat{\beta_{0s}} + \widehat{\beta_{1s}}TEMP + \widehat{\beta_{2s}}PREC + \widehat{\beta_{3s}}SRAD + \widehat{\beta_{4s}}eCO_2
\tag{11}
$$

$$
GPP = \sum_{s=1}^{4} GPP_s
\tag{12}
$$

The LUE GPP data are used for model calibration and validation. The model is calibrated using the data from 2001 to 2009 and the data from 2010 to 2018 are used to validate the model.

3.3. Attribution Analysis Method

The contributions of driving factors to GPP were calculated based on the ridge regressive coefficient and the trend of independent factor:

$$
\eta_c = a_c X_{c,trend}
\tag{13}
$$

where η_c is the contributions of influence factor to the GPP variation, a_c, $X_{c,trend}$ are the regressive coefficient and the normalized trend of the influence factors which is between 0 and 1.

The relative contribution of different driving factors to GPP could be confirmed by the following:

$$
\eta_{rc,i} = \frac{|\eta_{c,i}|}{|\eta_{c,1}| + |\eta_{c,2}| + |\eta_{c,3}| + \cdots}
\tag{14}
$$

where $\eta_{rc,i}$ is the relative contribution of X_i to the trend of GPP.

3.4. Future Scenarios and Downscaling

Four future scenarios comprehensively consider shared socio-economic paths (SSPs) and typical concentration paths (RCPs), namely SSP1-2.6, SSP2-4.5, SSP3-7.0, and SSP5-8.5. After evaluating the GCMs of CMIP6 in the Yangtze River Basin, four climate models (NorESM2-MM, ACCESS-CM2, IPSL-CM6A-LR, MPI-ESM1-2-LR) were selected by calculating correlation coefficient and standard deviation. Then, they were downscaled by quantile correction after collective average. The specific evaluation and correction methods are as follows:

$$
S = \frac{4(1+R)^4}{(\sigma_f + 1/\sigma_f)^2 (1+R_0)^4}
\tag{15}
$$

where R is the correlation coefficient and R_0 is the maximum correlation coefficient, σ_f is the specific value of standard deviation. The Quantile Mapping method is designed to reduce the difference between the empirical cumulative distribution functions (CDFs) of

the model data and that of the observation data by establishing transfer functions. Then, these transfer functions are used to correct the future climate model data. The transfer function can be expressed as

$$x_{mc} = F_{o,c}^{-1}\{F_{m,c}[x_{m,v}(t)]\} \tag{16}$$

where x_{mc} is the corrected climate model data; $x_{m,v}(t)$ is the original climate model data of t period; $F_{m,c}$ is the CDFs of original climate model data for historical periods; $F_{o,c}^{-1}$ is the inverse empirical CDFs of observation data.

4. Results

4.1. Model Validation

The R^2, NSE, and RMSE are calculated to evaluate the model performance as shown in Table 1. The results show that GPP could be captured quite well with the R^2, NSE, and RMSE which are 0.97, 0.97, and 11.03 $gCm^{-2}mon^{-1}$. It can also be seen from 11 catchments that the R^2 is higher than 0.9 in most catchments, except for that of the Poyang Lake, lower trunk stream, and Taihu Lake within the values about 0.85. The NSE values in most of the subbasins are higher than 0.9, except for the Dongting Lake, Poyang Lake, lower trunk stream, and Taihu Lake within the values around 0.8. The RMSE of most basins are lower than 20 $gCm^{-2}mon^{-1}$, except for that of the Wujiang River, Poyang Lake, lower trunk stream, and Taihu Lake which are lower than 25 $gCm^{-2}mon^{-1}$. Figure 3 shows the spatial patterns of GPP in different seasons between the model simulated GPP and LUE GPP. The results show that the simulated GPP could reflect the spatial distribution pattern of GPP in different seasons well. In addition, it can be seen that the LUE-RE model could capture the interannual and seasonal variations quite well with good agreement between the simulated and LUE-based GPP from Figure 4. Overall, the model results are acceptable for GPP simulations in the Yangtze River.
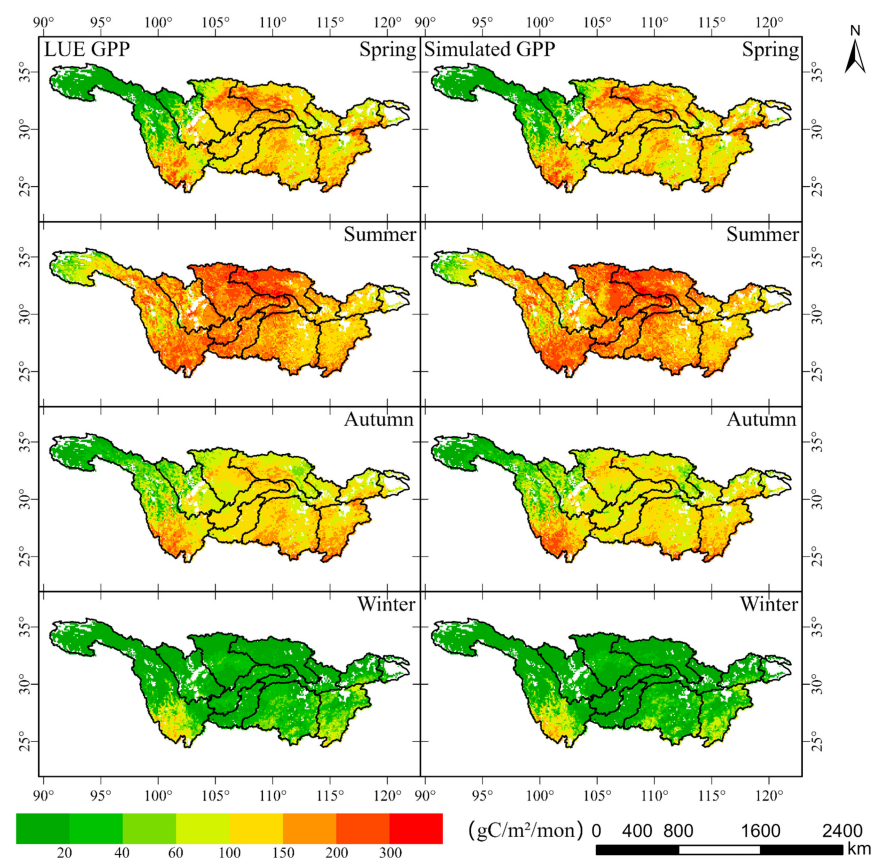

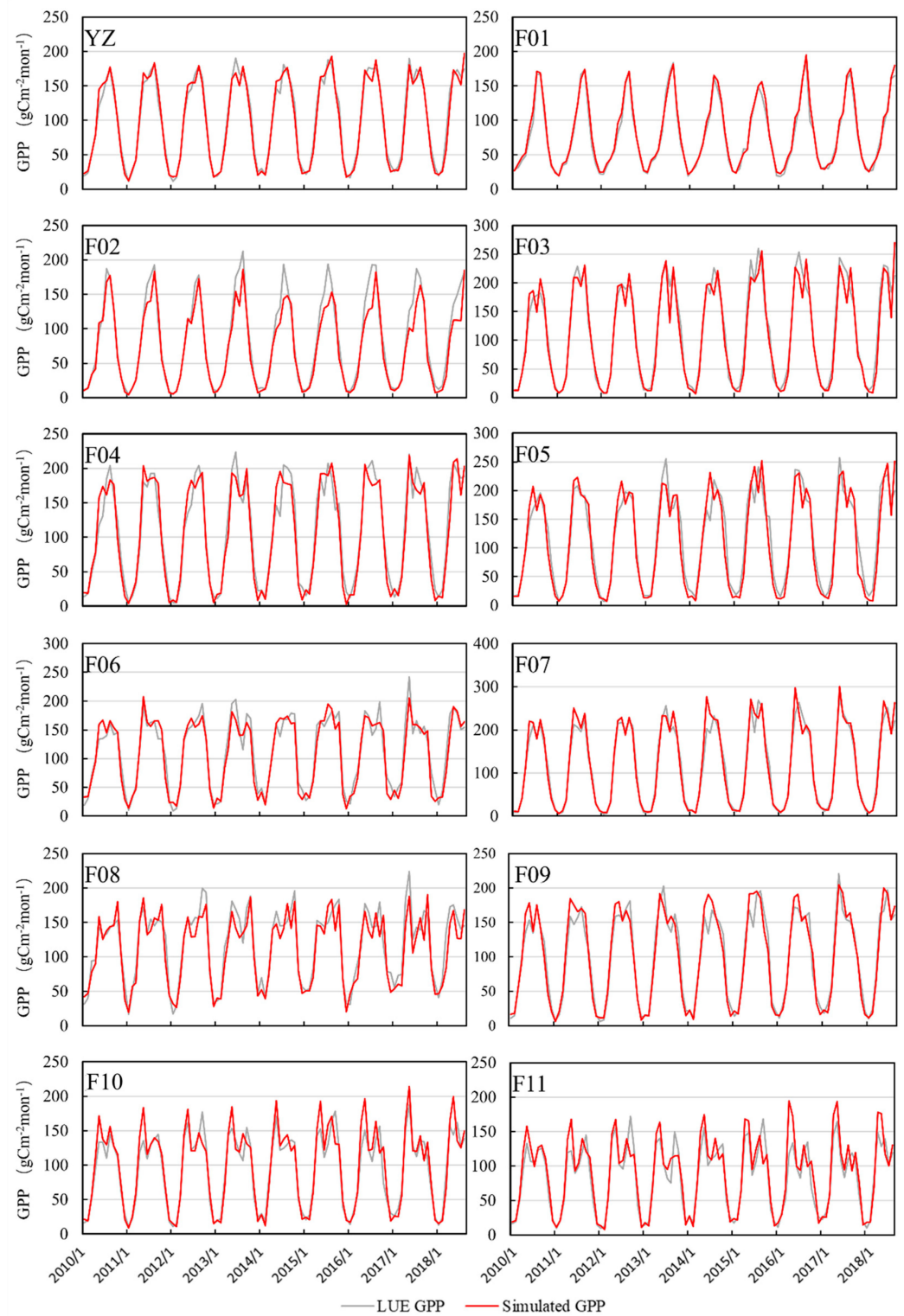**Figure 3.** Spatial comparison between simulated GPP and LUE GPP.

Figure 4. Comparison of monthly GPP changes between model simulation values and LUE GPP in the Yangtze River and 11 sub basins.

Table 1. Model performance in monthly GPP simulation by LUE-RE model.

Sub Basins	R^2	NSE	RMSE $(gCm^{-2}mon^{-1})$
Yangtze River	0.97	0.97	11.03
Jinsha River	0.98	0.98	7.38
Mintuo River	0.93	0.90	19.35
Jialing River	0.95	0.95	18.00
Wujiang River	0.93	0.91	21.24
Upper trunk stream	0.94	0.92	20.90
Dongting Lake	0.90	0.89	19.93
Hanjiang River	0.96	0.95	20.15
Poyang Lake	0.85	0.81	21.97
Middle trunk stream	0.93	0.92	16.61
Lower trunk stream	0.85	0.81	21.87
Taihu Lake	0.85	0.76	22.19

4.2. Attributions of Historical GPP Changes

(1)   Spatial and temporal variation of historical GPP

The changes in annual GPP in the different sub basins of the Yangtze River Basin are illustrated in Figure 5. In the whole Yangtze River, GPP increases with a slope of 9.18 $gCm^{-2}year^{-1}a^{-1}$, and it shows obvious growth trends in the Jialing River, Wujiang River, upper trunk stream, Dongting Lake and Poyang Lake, with the slopes of 15.74 $gCm^{-2}year^{-1}a^{-1}$, 11.16 $gCm^{-2}year^{-1}a^{-1}$, 14.49 $gCm^{-2}year^{-1}a^{-1}$, and 12.67 $gCm^{-2}year^{-1}a^{-1}$, respectively, while in Taihu Lake, GPP shows less growth trend within the slope of 1.35 $gCm^{-2}year^{-1}a^{-1}$. In general, the GPP in the Yangtze River Basin shows an increasing trend, but the increasing trends are different in different sub basins.

The spatial distribution of GPP is shown in Figure 6. In spring and autumn, the GPP in the Yangtze River Basin is mostly concentrated around 150 $gCm^{-2}mon^{-1}$; in summer, GPP is mostly concentrated around 300 $gCm^{-2}mon^{-1}$; in winter, the GPP is mostly less than 40 $gCm^{-2}mon^{-1}$. The regions with high GPP values are concentrated in the southwest and southeast of the Yangtze River Basin, Jialing River, and Hanjiang River.

To further identify the historical trends of GPP changes in the Yangtze River Basin during different seasons, the slopes of the monthly mean GPP changes in different seasons are investigated as shown in Figure 7. The results show that the changing trends of GPP in the Yangtze River Basin are most obvious in spring, and the regions with significant increases occupy a large space, among which the growth trend is most significant in the Jialing River, Hanjiang River, and the upper trunk stream at greater than 3 $gCm^{-2}mon^{-1}a^{-1}$; in summer, the regions with significant growth are only concentrated in the Jinsha River, Jialing River, and part of Hanjiang River, while Dongting Lake and Poyang Lake have a certain decreasing trend. In autumn, the regions with significant increases are concentrated in the southwest of the Yangtze River Basin, with a growth slope of 2–3 $gCm^{-2}mon^{-1}a^{-1}$. In winter, the growth trend of GPP in the entire basin is slight and concentrated at 0–1 $gCm^{-2}mon^{-1}a^{-1}$.
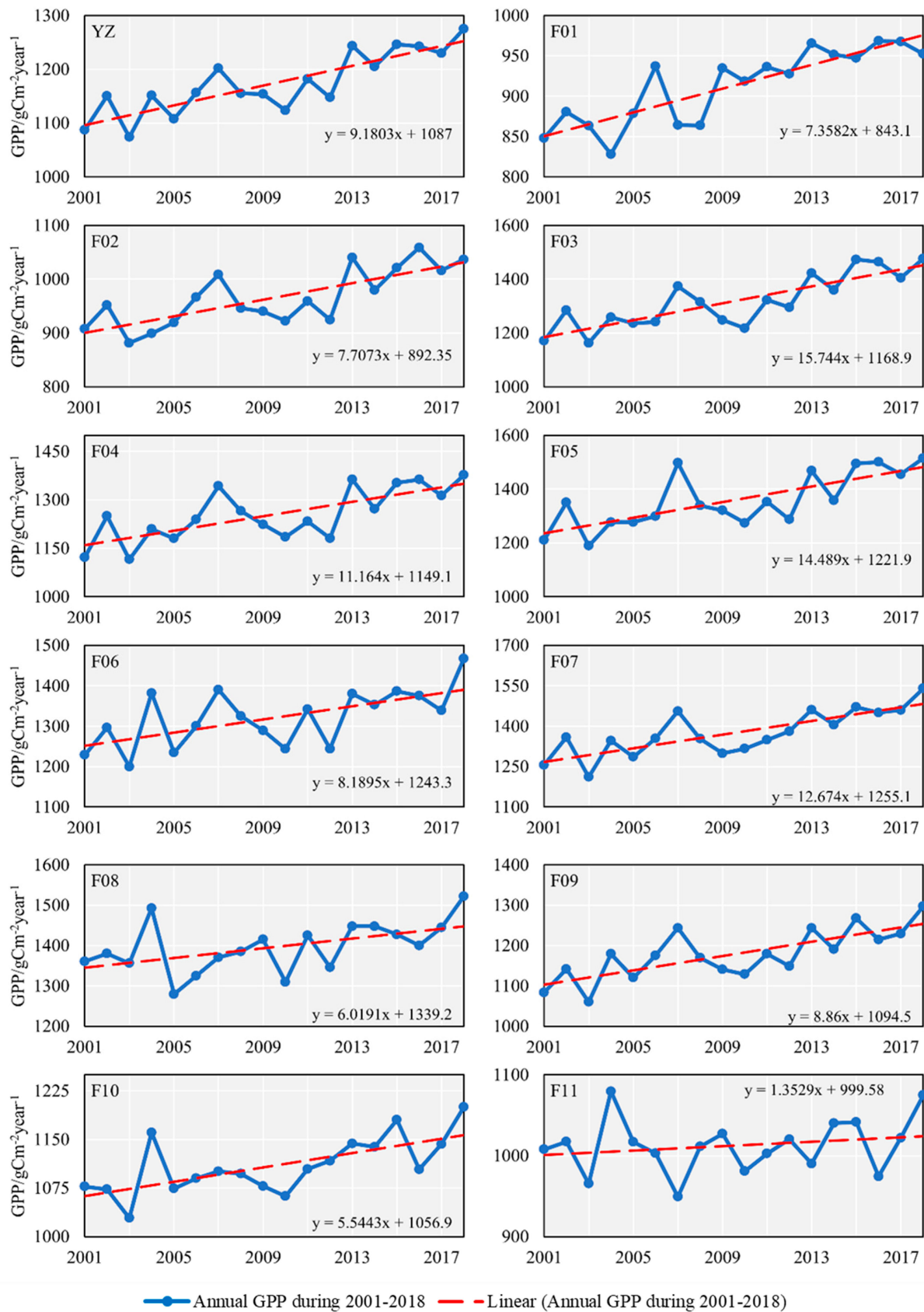
Figure 5. Changes of annual gross primary productivity in the Yangtze River Basin.
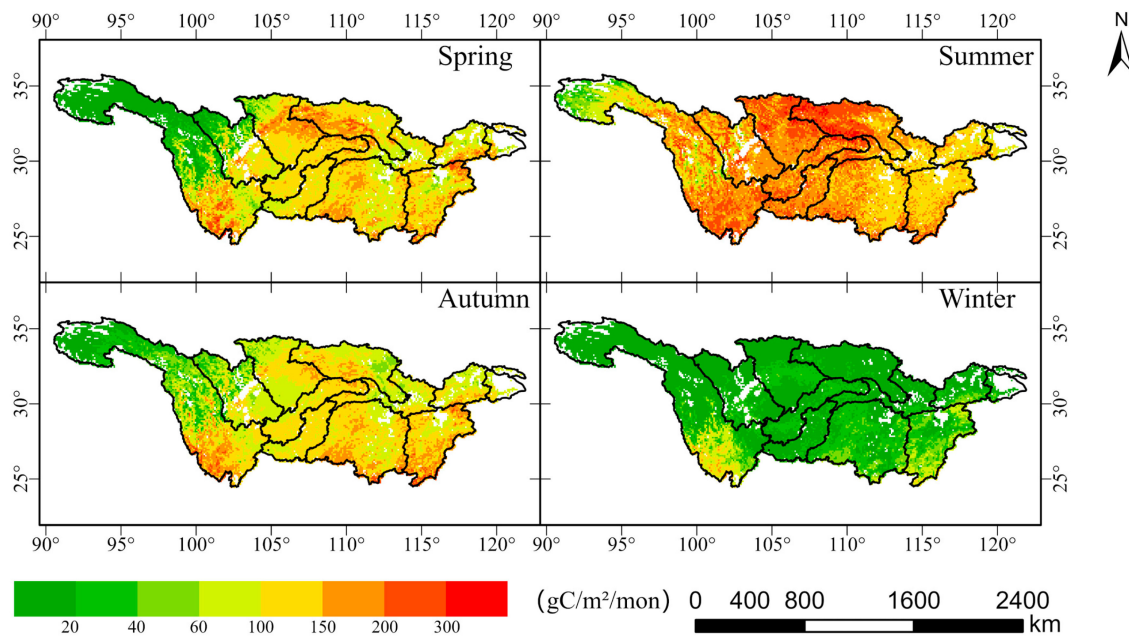
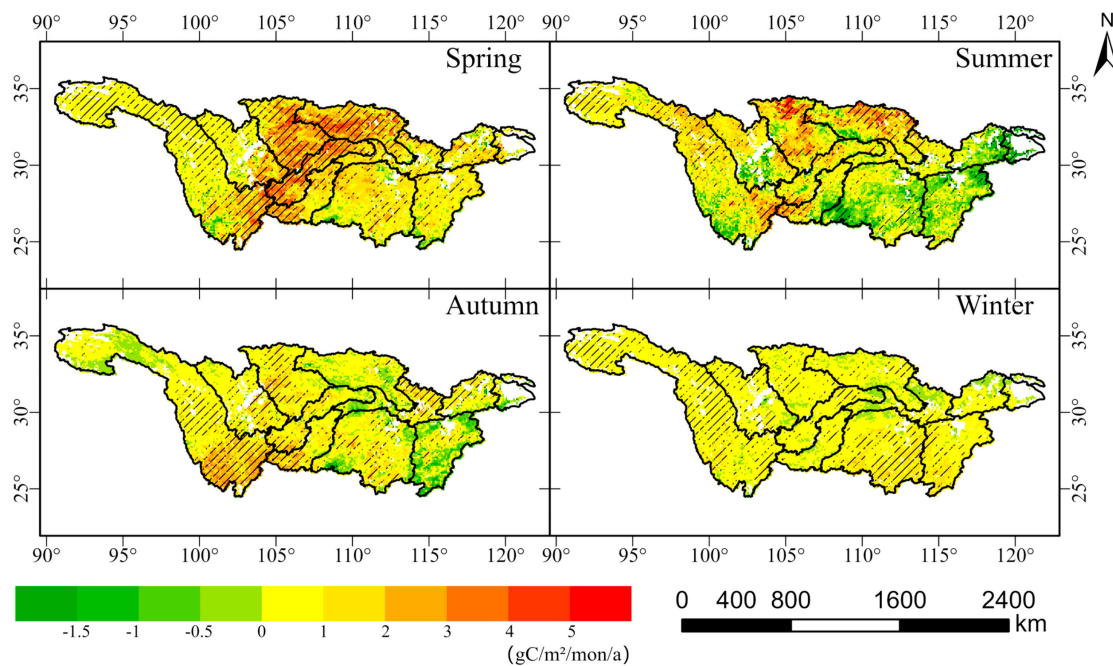**Figure 6.** The spatial pattern of GPP in different seasons.

Figure 7. Changes of seasonal GPP (the stripes areas indicating significant changes).

(2)   Sensitivities of GPP to different climate factors

The sensitivities of monthly GPP to different climate factors are shown in Figure 8. Figure 8a shows that GPP increases as CO_2 enrichment in nearly all the months, and GPP is most sensitive to elevated CO_2 in spring (April, May) and October, November, and December in the Yangtze River Basin. The highest sensitivity coefficient ranges between 0.389 (Jinsha River) and 0.651 (Jialing River) in the basin. The sensitivity of GPP to temperature (TEMP) changes is shown in Figure 8b indicating an obvious negative correlation from late spring (May) to autumn (October) and positive correlation from winter (November) to spring (April) in most subregions. The highest positive coefficient ranges between 0.25 (Taihu Lake) and 0.683 (Hanjiang River), while the lowest negative coefficient ranges

between -0.948 (upper trunk stream) and -0.378 (Taihu Lake). The sensitivity of GPP to precipitation (PREC) shows more complexity with significant spatial–temporal variance with both positive and negative correlation ranges between -0.34 and 0.32. Figure 8d shows the sensitivity of GPP to solar radiation. The results show almost a positive trend with solar radiation (SRAD) in the basin and it is most sensitive to solar radiation from May to November, especially in the Jialing River (0.893), Wujiang River (0.765), upper trunk stream (0.799), Dongting Lake (0.737), Hanjiang River (0.843), and Poyang Lake (0.763).

Figure 8. Sensitivity of GPP to elevated CO_2 (**a**), TEMP (**b**), PREC (**c**), SRAD (**d**) in different sub basins.

(3)   Attributions of annual GPP changes

The contribution of different climate factors to GPP in the Yangtze River Basin is shown in Figures 9 and 10. It can be seen that elevated CO_2 is the main driving factor contributing most of the positive effects in the Yangtze River Basin. The positive contribution to GPP is relatively high in the entire basin, with an average of 60%, and 25% of pixels contribute less than 55% to GPP. The contribution of 25% to 75% of pixels to GPP ranges from 55% to 80%, and the contribution of 25% of pixels to GPP is greater than 75%. The average contribution of temperature to GPP is about 4%. The positive contribution is relatively large at the source of the Yangtze River and concentrated in the Jinsha River system. In other regions, the main negative contribution is relatively large, with negative pixels accounting for about 60%, 25% of pixels contributing less than -10% to GPP, 25% to 75% of pixels contributing between -10% to GPP, and 25% of pixels contributing more than -3% to GPP. The contribution of precipitation to GPP is relatively small, with an average value of 0.3%. Positive and negative performance accounts for 50%, with 25% of pixels contributing less than -3%, 25% to 75% contributing between -3% and 4%, and 25% contributing more than 4%. The contribution of solar radiation to GPP is mainly negative with an average value of -5%. Negative contribution pixels account for 65%, 25% of pixels contribute less

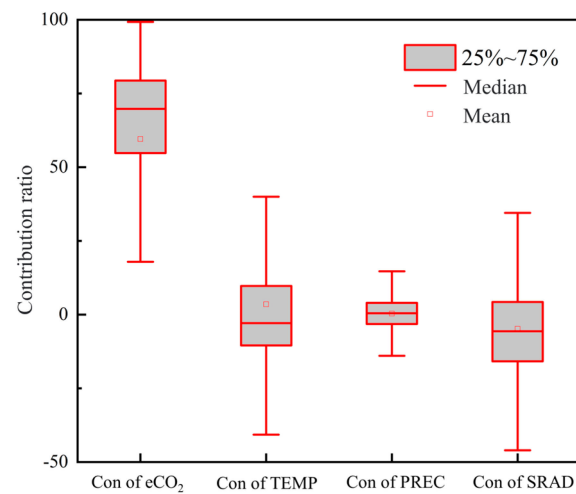than −16%, 25% to 75% contribute between −16% and 4%, and 25% contribute more than 4% to GPP.

Figure 9. The box plot of elevated CO_2 (eCO_2), TEMP, PREC, and SRAD contribution to GPP.
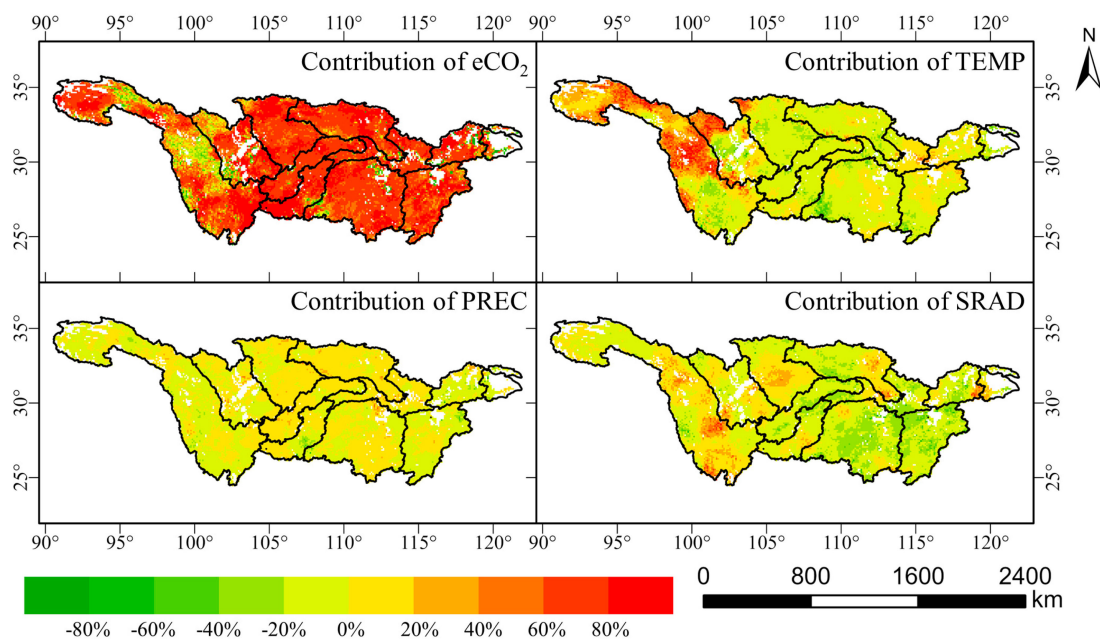

Figure 10. Spatial distribution map of elevated CO_2 (eCO_2), TEMP, PREC, and SRAD contribution to GPP.

(4)　Attributions of seasonal GPP changes

The contribution of different climate factors to seasonal GPP is shown in Figure 11. It can be seen that elevated CO_2 is the dominant factor contributing large GPP increases in nearly all the subregions except for that in the summer of the downstream main stream and the summer and winter of the Taihu Lake system. The contribution of elevated CO_2 to GPP in autumn and winter is basically higher than that in summer. The average contributions of elevated CO_2 to seasonal GPP are 62.84%, 32.6%, 60.5%, and 46.3% in spring, summer, autumn, and winter, respectively. The relative contribution of TEMP to GPP is generally negative in summer and positive in other seasons; in particular, the negative effects could reach above −20% in six subregions. The relative contributions of TEMP to GPP are 12.63%, −0.06%, 1.06%, and 5.17% in the four seasons. The contribution of PREC to GPP is mainly negative in autumn and low in other seasons. In spring, summer, and winter, the average

contribution of PREC to GPP is about −4.99%, 1.74%, and 0.69%. Meanwhile, in autumn, the average contribution of PREC to GPP is −24.2% and it could reach about −36% in the Hanjiang River. The contribution of SRAD to GPP is mainly negative in autumn and low in other seasons. The average contribution of SRAD to GPP in spring is −2.98% and is 2.62% in summer. In winter, the average contribution of SRAD to GPP is much higher, about −22.64%, and the largest negative effect is nearly −30%; in winter, the average contribution of SRAD to GPP is relatively lower, about 2.91%. Overall, the contributions of different climate factors to GPP in the Yangtze River Basin show large differences. The positive contribution of elevated CO_2 changes to GPP is significant, particularly in spring and autumn, while the positive contributions of TEMP, PREC, and SRAD to GPP changes are relatively smaller. Moreover, it should be mentioned that TEMP makes a significant negative contribution to GPP in summer, while PREC and SRAD make a significant negative contribution to GPP in autumn.
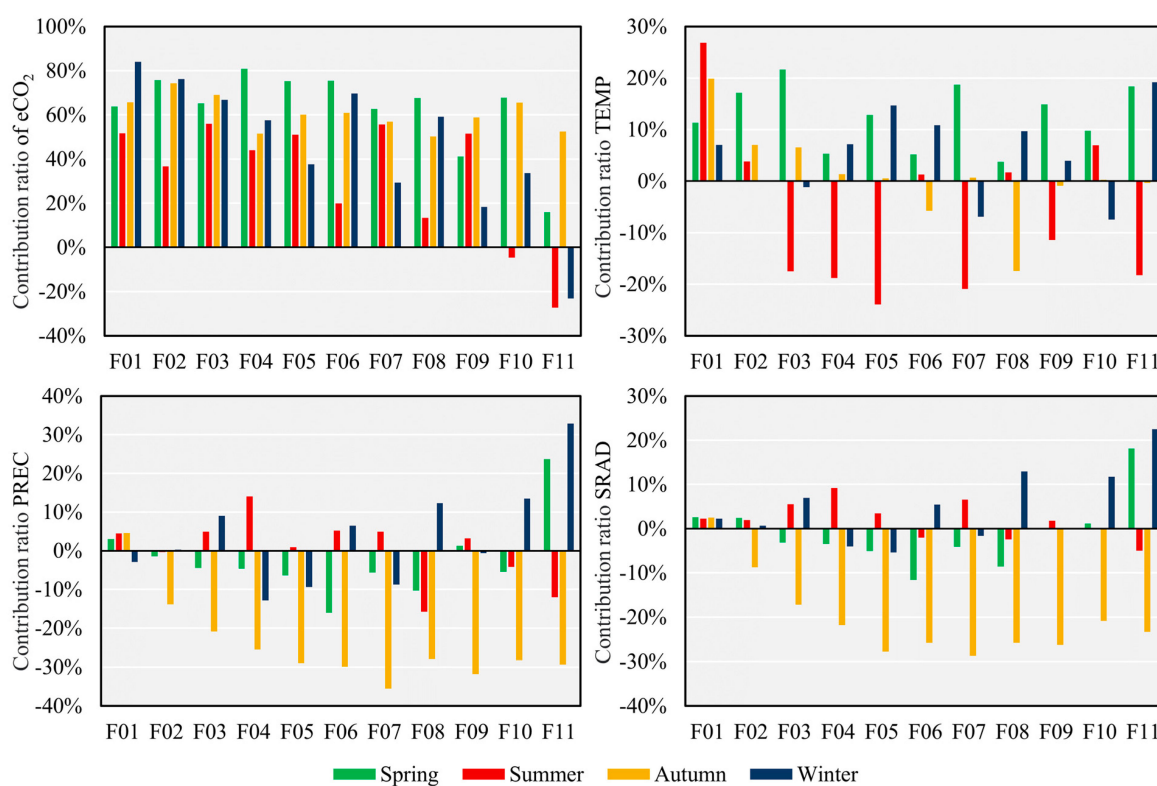

Figure 11. The contribution of elevated CO_2 (eCO_2), TEMP, PREC, and SRAD to GPP in different seasons.

4.3. Future Projection of GPP Changes under Different Scenarios

(1)   Projected temporal patterns of annual and seasonal GPP

The projected GPP changes spanning 2014 to 2100 in the Yangtze River Basin are shown in Figure 12. It is evident that substantial disparities exist in the future alterations of the Yangtze River Basin under different climate model scenarios. Among them, GPP shows an increasing trend and then a decreasing trend under the SSP1-2.6 scenario, while GPP shows a continuous increasing trend under other scenarios, and the growth amplitude is SSP5-8.5 > SSP3-7.0 > SSP2-4.5. From the perspective of different seasons, the slope of GPP growth in spring is the highest, followed by autumn, and the lowest in winter. Due to the rapid growth of GPP in spring, GPP in spring will be higher than that in summer around 2050 under the SSP2-4.5, SSP3-7.0, and SSP5-8.5 scenarios. It is evident that the growth rate of GPP exhibits variations across different stages in the future, thus necessitating a division of the future into three distinct phases: S1 stage from 2014 to 2040, S2 stage from 2041 to 2070, and S3 stage from 2071 to 2100. From the slope changes of different

seasons in different stages (Figure 13), it can be seen that GPP growth is predominantly concentrated during spring and autumn across various scenarios, with spring displaying the most pronounced growth trend. And the growth trend in winter is the smallest. Under the SSP1-2.6 scenario, the growth trend of GPP in S1 stage is the most pronounced, with 1.77 $gCm^{-2}mon^{-1}a^{-1}$ in spring, 0.82 $gCm^{-2}mon^{-1}a^{-1}$ in summer, 1.06 $gCm^{-2}mon^{-1}a^{-1}$ in autumn, and 0.42 $gCm^{-2}mon^{-1}a^{-1}$ in winter; the growth trend of GPP in the S2 stage has decreased to a certain extent, but it still maintains a relatively low increase trend, with 0.40 $gCm^{-2}mon^{-1}a^{-1}$ in spring, 0.16 $gCm^{-2}mon^{-1}a^{-1}$ in summer, 0.22 $gCm^{-2}mon^{-1}a^{-1}$ in autumn, and 0.14 $gCm^{-2}mon^{-1}a^{-1}$ in winter; during the S3 stage, GPP showed a downward trend, with -0.58 $gCm^{-2}mon^{-1}a^{-1}$ in spring, -0.29 $gCm^{-2}mon^{-1}a^{-1}$ in summer, -0.36 $gCm^{-2}mon^{-1}a^{-1}$ in autumn, and -0.13 $gCm^{-2}mon^{-1}a^{-1}$ in winter. Under the SSP2-4.5 scenario, the trend of GPP changes in S1 and S2 stages is basically similar, with 1.93 and 2.00 $gCm^{-2}mon^{-1}a^{-1}$ in spring, 0.89 and 0.92 $gCm^{-2}mon^{-1}a^{-1}$ in summer, 1.37 and 1.34 $gCm^{-2}mon^{-1}a^{-1}$ in autumn, and 0.45 and 0.48 $gCm^{-2}mon^{-1}a^{-1}$ in winter, respectively; the growth trend of GPP in S3 stage has decreased to a certain extent, with 0.83 $gCm^{-2}mon^{-1}a^{-1}$ in spring, 0.43 $gCm^{-2}mon^{-1}a^{-1}$ in summer, 0.53 $gCm^{-2}mon^{-1}a^{-1}$ in autumn, and 0.23 $gCm^{-2}mon^{-1}a^{-1}$ in winter. Under the SSP3-7.0 scenario, the GPP growth trend from S1 to S3 stages continues to increase, with values of 2.39, 3.56, and 4.73 $gCm^{-2}mon^{-1}a^{-1}$ in spring, 0.97, 1.53, and 2.07 $gCm^{-2}mon^{-1}a^{-1}$ in summer, 1.47, 2.35, and 3.10 $gCm^{-2}mon^{-1}a^{-1}$ in autumn, and 0.58, 0.82, and 1.06 $gCm^{-2}mon^{-1}a^{-1}$ in winter, respectively. Under the SSP5-8.5 scenario, the growth trend of GPP from S1 to S3 stages continues to increase, and the growth amplitude is greater than that of the SSP3-7.0 scenario, with 2.64, 5.31, and 8.61 $gCm^{-2}mon^{-1}a^{-1}$ in spring, 1.16, 2.33, and 3.84 $gCm^{-2}mon^{-1}a^{-1}$ in summer, 1.71, 3.55, and 5.61 $gCm^{-2}mon^{-1}a^{-1}$ in autumn, and 0.62, 1.27, and 1.90 $gCm^{-2}mon^{-1}a^{-1}$ in winter, respectively.
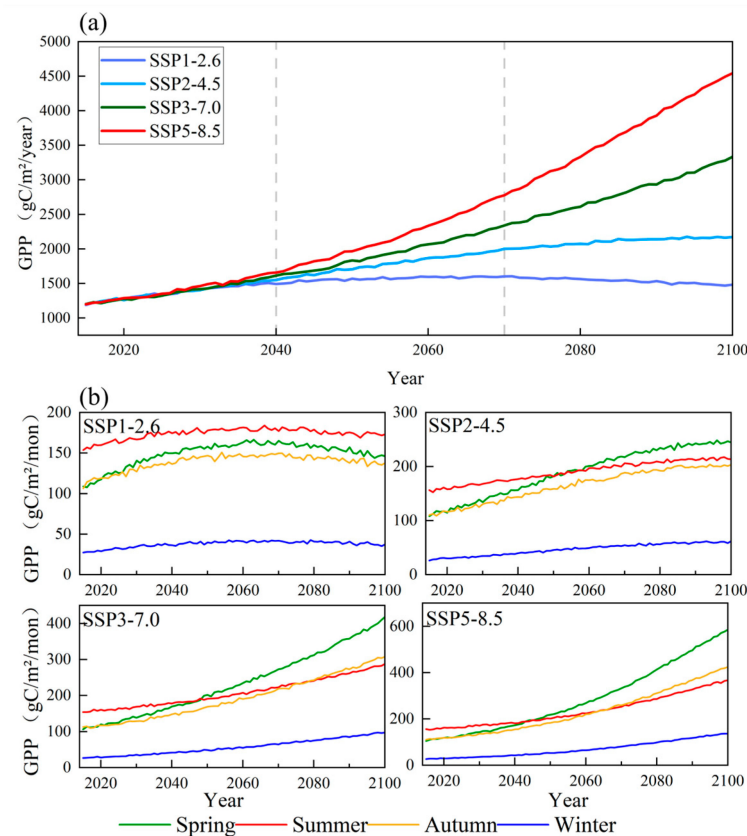

Figure 12. Projected future annual GPP (**a**) and seasonal GPP (**b**) changes in the Yangtze River Basin under different scenarios.
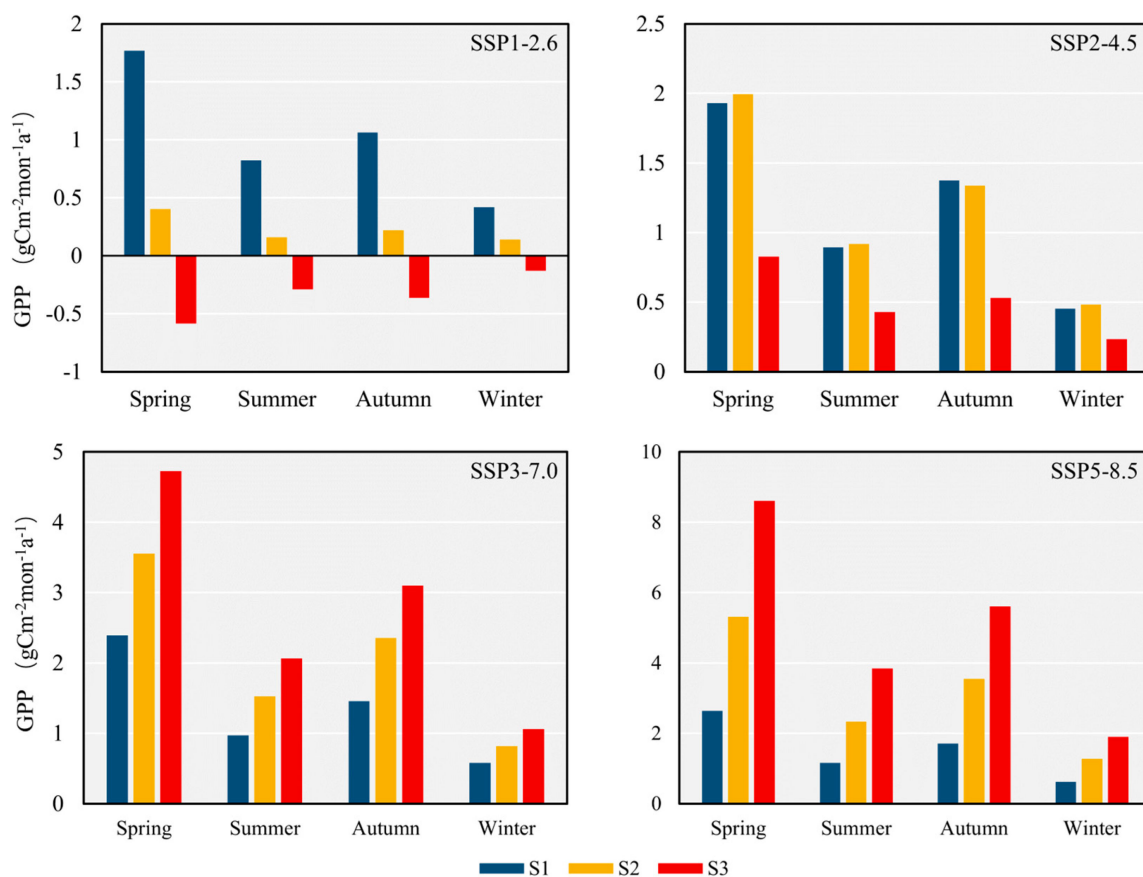
Figure 13. Slopes of seasonal GPP changes in the Yangtze River Basin under different scenarios.

(2)   Projected spatial patterns of annual and seasonal GPP

The annual average GPP in different seasons under different scenarios are as shown in Figure 14. Under SSP1-2.6 scenario, the following is shown: in spring, the area below 100 $gCm^{-2}mon^{-1}$ accounts for about 25%, and most of them are concentrated in the Jinsha River, the area between 100~200 $gCm^{-2}mon^{-1}$ accounts for about 45%, and the area above 200 $gCm^{-2}mon^{-1}$ accounts for about 30%, most of which are concentrated in the Jialing River, the upper trunk stream, and the Hanjiang River. In summer, the area below 100 $gCm^{-2}mon^{-1}$ accounts for about 10%; the area between 100 and 200 $gCm^{-2}mon^{-1}$ accounts for about 50%, most of which are concentrated in the Poyang Lake and Dongting Lake; the area above 200 $gCm^{-2}mon^{-1}$ accounts for about 40%, most of which are concentrated in the Mintuo River, Jialing River, and Hanjiang River. In autumn, the area below 100 $gCm^{-2}mon^{-1}$ accounts for about 25%, and most of them are concentrated in the Jinsha River; the area between 100~200 $gCm^{-2}mon^{-1}$ accounts for about 55%, and the area above 200 $gCm^{-2}mon^{-1}$ accounts for about 20%, most of which are concentrated in the southwest of the basin, the upper trunk stream, Dongting Lake, and Poyang Lake; in winter, 90% of areas have GPP below 100 $gCm^{-2}mon^{-1}$, while areas with higher GPP are mainly distributed in the southern part.

Under SSP2-4.5 scenario, the following is shown: in spring, the area below 100 $gCm^{-2}mon^{-1}$ accounts for about 20%, and most of them are concentrated in the Jinsha River; the area between 100–200 $gCm^{-2}mon^{-1}$ accounts for about 20%, and the area above 200 $Cm^{-2}mon^{-1}$ accounts for about 60%, which is mainly concentrated in the Jialing River, the upper trunk stream, and the Hanjiang River. In summer, the area below 100 $gCm^{-2}mon^{-1}$ accounts for about 10%; the area between 100 and 200 $gCm^{-2}mon^{-1}$ accounts for about 40%, mostly concentrated in the Poyang Lake and Dongting Lake, and the area above 200 $gCm^{-2}mon^{-1}$ accounts for about 50%, mostly concentrated in the Mintuo River, Jialing River, and Han-

jiang River. In autumn, the area below $100\ \mathrm{gCm^{-2}mon^{-1}}$ accounts for about 20%, and most of them are concentrated in the Jinsha River; the area between $100\sim200\ \mathrm{gCm^{-2}mon^{-1}}$ accounts for about 30%, and the area above $200\ \mathrm{gCm^{-2}mon^{-1}}$ accounts for about 50%, and most of them are concentrated in the southwest of the basin, the upper trunk stream, Dongting Lake, and Poyang Lake; in winter, 85% of regions have GPP below $100\ \mathrm{gCm^{-2}mon^{-1}}$.

Under SSP3-7.0 scenario, the following is shown: in spring, the area below $100\ \mathrm{gCm^{-2}mon^{-1}}$ accounts for about 20%, and most of them are concentrated in the Jinsha River; the area between $100-200\ \mathrm{gCm^{-2}mon^{-1}}$ accounts for about 20%, and the area above $200\ \mathrm{gCm^{-2}mon^{-1}}$ accounts for about 60%, which is mainly concentrated in the Jialing River, upper trunk stream, and Hanjiang River; in summer, the area below $200\ \mathrm{gCm^{-2}mon^{-1}}$ accounts for about 50%, mostly concentrated in the Poyang Lake, Dongting Lake, and the lower reaches of the Yangtze River; the area between 200 and $300\ \mathrm{gCm^{-2}mon^{-1}}$ accounts for about 20%, mostly concentrated in the Jinsha River; the area above $300\ \mathrm{gCm^{-2}mon^{-1}}$ accounts for about 30%, mostly concentrated in the Jialing River and the Hanjiang River. In autumn, the area below $100\ \mathrm{gCm^{-2}mon^{-1}}$ accounts for about 20%, and most of them are concentrated in the Jinsha River; the area between $100\sim300\ \mathrm{gCm^{-2}mon^{-1}}$ accounts for about 60%, and the area above $300\ \mathrm{gCm^{-2}mon^{-1}}$ accounts for about 20%, most of which are concentrated in the southwest of the basin, the upper trunk stream, and Dongting Lake; in winter, 80% of regions have GPP below $100\mathrm{gCm^{-2}mon^{-1}}$.

Under SSP5-8.5 scenario, the following is shown: in spring, the area below $100\ \mathrm{gCm^{-2}mon^{-1}}$ accounts for about 15%, and most of them are concentrated in the Jinsha River; the area between $100\sim300\ \mathrm{gCm^{-2}mon^{-1}}$ accounts for about 15%, and the area above $300\ \mathrm{gCm^{-2}mon^{-1}}$ accounts for about 60%, most of which are concentrated in the Jialing River, upper trunk stream, and Hanjiang River. In summer, the area below $200\ \mathrm{gCm^{-2}mon^{-1}}$ accounts for about 40%, mostly concentrated in the Poyang Lake, Dongting Lake, and the lower reaches of the Yangtze River; the area between 200 and $300\ \mathrm{gCm^{-2}mon^{-1}}$ accounts for about 15%, mostly concentrated in the Jinsha River. The area above $300\ \mathrm{gCm^{-2}mon^{-1}}$ accounts for about 45%, mostly concentrated in the Jialing River and the Hanjiang River. In autumn, the area below $100\ \mathrm{gCm^{-2}mon^{-1}}$ accounts for about 20%, and most of them are concentrated in the Jinsha River; the area between $100\sim300\ \mathrm{gCm^{-2}mon^{-1}}$ accounts for about 40%, and the area above $300\ \mathrm{gCm^{-2}mon^{-1}}$ accounts for about 40%, and most of them are concentrated in the southwest of the basin, the upper trunk stream, and Dongting Lake; in winter, 70% of the regions have GPP below $100\ \mathrm{gCm^{-2}mon^{-1}}$.

To further investigate the variations in GPP across different sub basins of the Yangtze River Basin in the future, the changes between future and historical GPP are illustrated in Figure 15. Generally, GPP increases mostly in spring and autumn, while it shows less increase and even some decreases compared to the historical values in some sub basins in summer. In spring, the sub basins with large changes in GPP include the Jialing River, Wujiang River, upper trunk stream, and Hanjiang River, of which the upper trunk stream has the largest change, with 109.11, 193.24, 290.25, and $400.01\ \mathrm{gCm^{-2}mon^{-1}}$, respectively, under SSP1-2.6, SSP2-4.5, SSP3-7.0, and SSP5-8.5 scenarios. In summer, the sub basins with great changes of GPP include the Mintuo River, Jialing River, the upper trunk stream, and the Hanjiang River. The Mintuo River has the largest change of $54.95\ \mathrm{gCm^{-2}mon^{-1}}$ under SSP1-2.6 scenarios, and the Hanjiang River has the largest change of 86.45, 135.73, and $202.43\ \mathrm{gCm^{-2}mon^{-1}}$ under SSP2-4.5, SSP3-7.0, and SSP5-8.5 scenarios. Meanwhile, in the Dongting Lake, Poyang Lake, lower trunk stream, and Taihu Lake, GPP show small decreases compared to the historical values. In autumn, GPP shows large increases in the upper trunk streams within 77.69, 121.99, 167.74, and $230.92\ \mathrm{gCm^{-2}mon^{-1}}$ under the four scenarios, respectively. GPP in the Jinsha River, Mintuo River, and the Taihu Lake shows less changes, of which the Jinsha River has the smallest increases of about 32.03, 48.95, 68.18, and $89.24\ \mathrm{gCm^{-2}mon^{-1}}$ under the four scenarios, respectively. In winter, GPP increases mostly in the Dongting Lake and the Poyang Lake, of which the Poyang Lake has the largest change, with 37.81, 57.91, 79.83, $109.63\ \mathrm{gCm^{-2}mon^{-1}}$, respectively; meanwhile,

it shows less changes in the Taihu Lake with 6.15, 4.36, 0.42, and 0.86 gCm^{-2}mon^{-1} under the four scenarios, respectively.
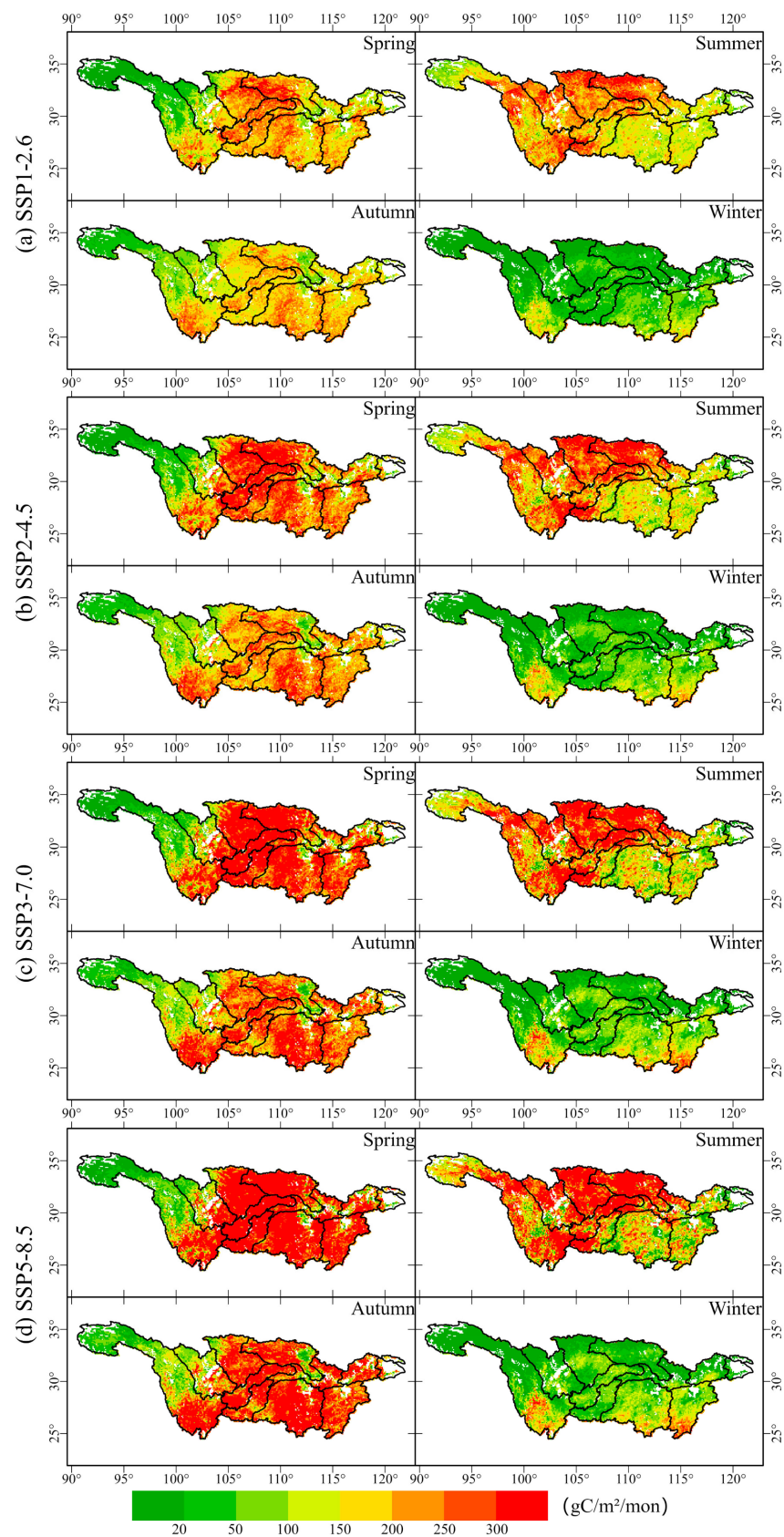

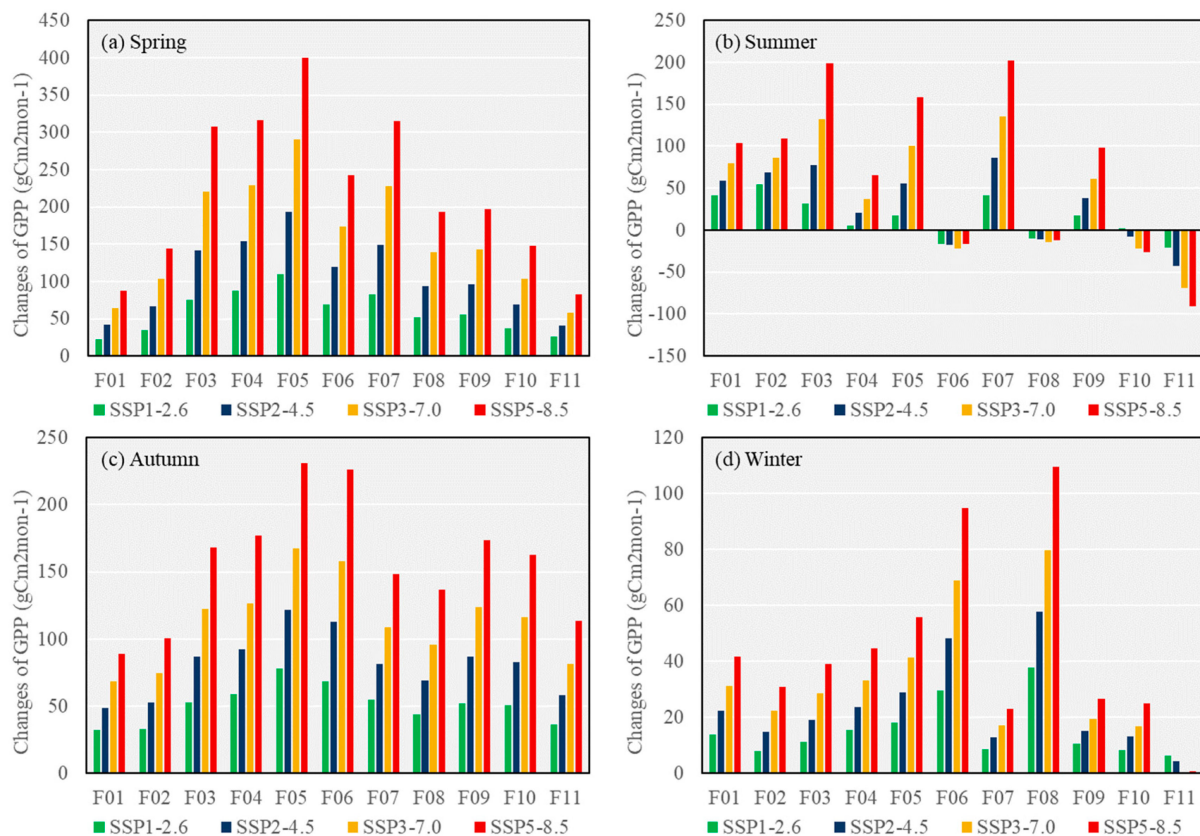**Figure 14.** The spatial distribution of projected future GPP under different scenarios.

Figure 15. Changes of future vs. historical GPP in different sub basins under different scenarios.

5. Discussion

5.1. Driving Factors on Historical GPP Variations

At annual scale, GPP shows an increasing trend in the Yangtze River Basin, which can be observed almost globally and is consistent with many previous studies [32,33]. However, GPP in the Yangtze River Basin does not maintain an increasing trend throughout the year at seasonal scale, and it increases mainly in April and May. Based on the sensitivity and contribution analysis of GPP, it can be seen that the main factor affecting the changes in GPP in spring is elevated CO_2, indicating that elevated CO_2 dominates the GPP changes in the Yangtze River Basin. At the same time, it can be seen that the impact of elevated CO_2 on GPP is mainly concentrated in spring and autumn, and the reason for the smaller increase in GPP in autumn is that the negative effects of precipitation and solar radiation offset a portion of the positive effects of elevated CO_2. From previous studies, it can also be seen that the fertilization effect of carbon dioxide is the most important factor in increasing vegetation productivity [34,35]. The increase in CO_2 concentration can enhance photosynthesis by controlling the closure of stomata and improving water use efficiency [36]. Figure 16 shows the correlations between the sensitivity of GPP to elevated CO_2 (deCO_2), temperature (dTEMP), precipitation (dPREC), and solar radiation (dSRAD) with temperature and precipitation in different months. It can be observed that the impact of elevated CO_2 on GPP is highest in spring when temperatures warm up and vegetation begins to grow. This may be due to the fertilization effect of carbon dioxide improving the water use efficiency of vegetation, leading to a significant increase in GPP. It can also be seen that in summer, when there is more precipitation, the correlation between deCO_2 and precipitation shows negative values. The more precipitation, the less obvious the response of GPP to carbon dioxide fertilization in regions, which can also prove that the fertilization effect of CO_2 mainly affects vegetation during periods of water scarcity. At the same time, there is also a certain correlation between deCO_2 and temperature, mainly showing a positive correlation,

which proves that an increase in temperature is beneficial for enhancing the fertilization effect of carbon dioxide. However, a negative correlation in summer also indicates that there is an optimal temperature. If the temperature is too high, it may inhibit the fertilization effect of carbon dioxide. In addition, the prolonged growth season of vegetation due to temperature rise further strengthens the fertilization effect of carbon dioxide.
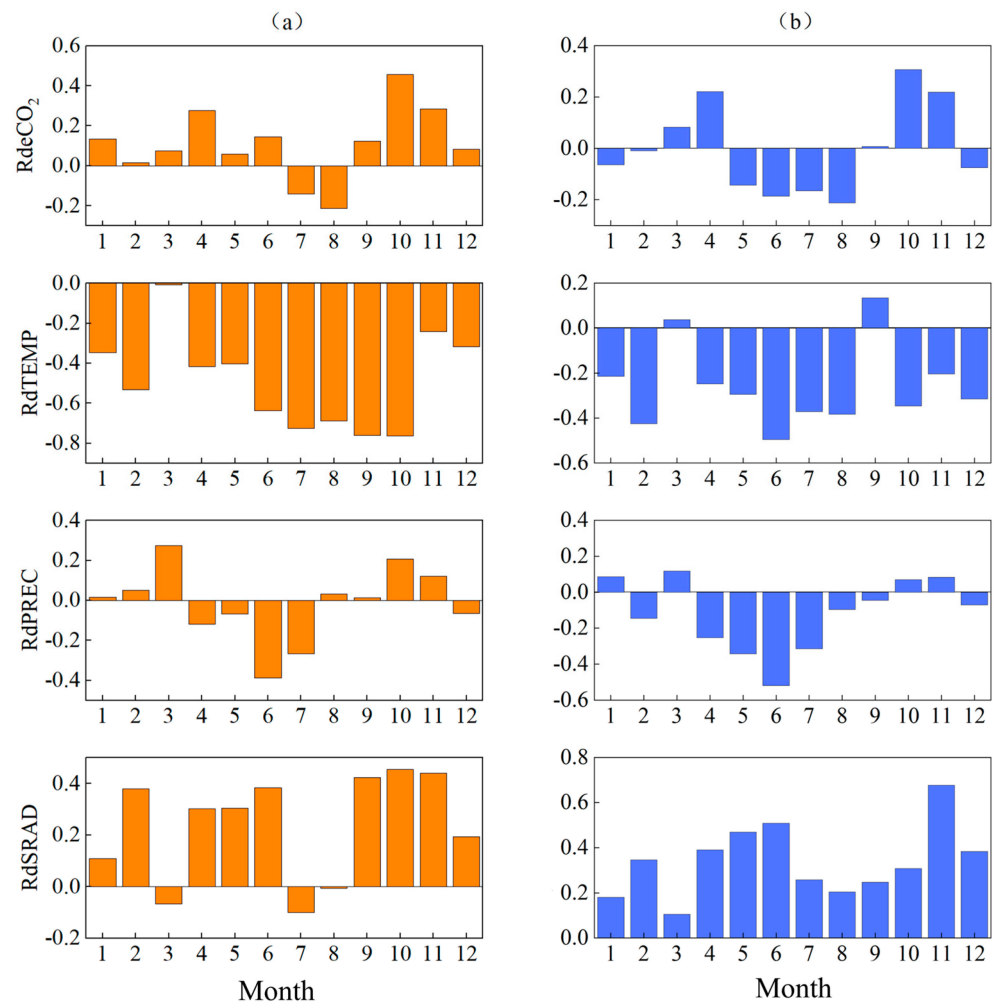

Figure 16. Correlation of elevated CO_2 (eCO_2), temperature, precipitation, and solar radiation with temperature (**a**) and precipitation (**b**) in the Yangtze River Basin.

Although changes in elevated CO_2 play a dominant role in vegetation change, the impact of climate variables on vegetation cannot be ignored. Many studies have shown that precipitation, temperature, and radiation are important factors affecting vegetation productivity. This study found that the sensitivity of GPP to precipitation is relatively low, mainly because the Yangtze River Basin has a large amount of precipitation, which is relatively humid, and the limiting effect of water on it is relatively low. From the correlation between dPREC and precipitation, it can be seen that they mainly show a negative correlation, proving that precipitation in areas with lower precipitation has a greater impact on vegetation productivity. It can also be found from other studies that precipitation plays a significant role in water-limited semi-arid ecosystems and is the main cause of vegetation changes [37]. Temperature affects various physiological processes of plants. Before reaching the optimal temperature, an increase in temperature usually increases plant photosynthesis and promotes plant growth. The dTEMP shows that the impact of temperature on GPP is the lowest in summer and is negative in most regions. Moreover, in summer, temperature also has a significant negative contribution to GPP, possibly due to climate warming. The

temperature in summer has exceeded the optimal temperature for vegetation, and the continued temperature increase will not promote vegetation growth. Combined with the correlation analysis between dTEMP and temperature, it can be proven that the impact of temperature on vegetation GPP is greater in areas with lower temperatures. In addition, an increase in temperature may also lead to an extension of vegetation growth period, thereby improving vegetation productivity [38], and it is more obvious in high-latitude and high-altitude regions [39], which can also be proven from the above conclusion. From the negative correlation between dTEMP and precipitation, it can be seen that precipitation may also inhibit the impact of temperature on vegetation. Solar radiation affects various aspects of vegetation growth and development through photosynthetic, thermal, and morphological effects, making it a key control factor for the vegetation sensitivity index, especially in humid climate areas with relatively low radiation levels [40,41]. The dSRAD is higher in rainy summers, and it is positively correlated with precipitation in all months, further supporting this conclusion. However, due to the combustion of fossil fuels, the aerosol load increases, leading to a decrease in solar radiation, which is also the reason for the negative contribution of solar radiation to GPP.

5.2. GPP Changes in the Future

In the future, GPP shows a significant upward trend, indicating that the carbon sequestration capacity of the Yangtze River Basin is constantly increasing. It can be clearly observed that under the SSP1-2.6 scenario, the GPP shows a downward trend from rapid growth to slow growth, indicating that the maintenance of stable or even decreasing elevated CO_2 leads to a decrease in the fertilization effect of CO_2, and the decrease in elevated CO_2 also leads to the maintenance of stable temperature, further weakening the negative effects of spring and autumn temperatures on vegetation, and alleviating the pressure of summer high temperatures on GPP. While under other scenarios, GPP increases with the continuous increase in elevated CO_2. From the future trends of GPP changes in the four scenarios, it can be seen that the changes in GPP are almost consistent with the changes in elevated CO_2. Over the past century, the terrestrial biosphere has responded to anthropogenic carbon dioxide emissions with the greatest increase in photosynthetic activity, which is proportional to the increase in atmospheric carbon dioxide concentration [42]. This phenomenon of GPP proportional to the increase in atmospheric elevated CO_2 will continue in the future, and elevated CO_2 will still dominate the changes in GPP. This is mainly because the increase in elevated CO_2 leads to a significant improvement in photosynthesis and water use efficiency at the leaf level of vegetation, and this change may alleviate the impact of future drought stress on vegetation [43].

The future growth of GPP in the Yangtze River Basin will be most significant in spring and autumn, partly due to the fertilization effect of elevated CO_2, and partly due to the positive impact of temperature rise. The increase in temperature will prolong the growth season of vegetation, leading to a larger leaf area in earlier spring and delaying the aging time of vegetation in autumn, resulting in a longer growth cycle of vegetation [44], combined with the fertilization effect of elevated CO_2, resulting in the highest growth trend of GPP in spring and autumn. In other stable climate conditions, vegetation will be within a specific temperature range, below the optimal temperature. Increasing temperature can promote enzyme activity, but beyond this temperature range, excessive heat can lead to stomatal closure and enzyme inactivation [45]. In summer, as the optimal temperature has already been exceeded, future high temperatures may have a significant negative impact on GPP, and the increasing temperature may have an increasing negative impact on vegetation, resulting in a lower growth rate of GPP. However, high concentrations of CO_2 can still bring positive effects to GPP growth in summer, and the positive effect of this CO_2 is higher than the negative impact of temperature rise, resulting in GPP being able to maintain an increasing level during the summer.

The growth of GPP may lead to an increase in evapotranspiration, or affect runoff, resulting in a decrease in runoff [46]. Based on the above results, it can be seen that the

vegetation productivity in the Yangtze River Basin will continue to increase under the conditions of climate change in the future, which may also lead to changes in hydrological processes. This situation may be more severe in spring, and the increase in vegetation productivity indicates that the water demand of future vegetation may increase, leading to an increase in transpiration, affecting water infiltration, and ultimately leading to a decrease in runoff. At the same time, due to the low precipitation in spring, it may cause the occurrence of drought events. Although there is more precipitation in summer, the risk of drought may also be further exacerbated by future temperature increases and increased vegetation productivity. Under different scenarios, the spring drought risk in the Yangtze River Basin may increase in sequence under SSP1-2.6, SSP2-4.5, SSP3-7.0, and SSP5-8.5. This drought risk needs to be especially prevented in the Jialing River, the Wujiang River, the upper trunk stream, and the Dongting Lake. It is worth noting that with the maintenance and increase in elevated CO_2, this potential drought risk may further intensify.

5.3. Uncertainties and Limitations

Due to the limitations of the statistical models, there are still some uncertainties of this research. In this study, climate factors and land cover are considered to build the LUE-RE model; however, other factors like topographic characteristics, soil type, and human activities would also affect future GPP changes, which were not considered and may result in certain uncertainties in GPP predictions. Furthermore, with the continuous increase in elevated CO_2, the fertilization effect of CO_2 on vegetation may be weakened, and the response of GPP to the increase in CO_2 concentration shows a nonlinear near-saturation feature [47]. The positive impact of increasing CO_2 concentration on terrestrial carbon absorption may be reduced [48]. This indicates that the response of GPP to elevated CO_2 may decrease in the future, which is an issue that the LUE-RE model did not consider and may lead to overestimation of the simulated GPP. Research has shown that by the end of the 21st century, the average temperature in tropical regions will exceed the optimal temperature, affecting vegetation photosynthesis. From our results, it can also be seen that as the future temperature increases, spring and autumn may have already reached the current summer temperature, leading to a change in the impact of temperature on GPP, which may also lead to a degree of overestimation of the simulated values. The above factors may lead to increasing uncertainties in the model at a larger time scale in the future.

6. Conclusions

In this study, a new method for estimating GPP by coupling the LUE model and regression model is developed, and the model could perform well in GPP simulation in the Yangtze River Basin. The main conclusions are as follows: (1) GPP in the Yangtze River Basin shows a significant increase trend in the historical period. The elevated CO_2 dominates the change of GPP in the Yangtze River Basin. (2) The growth trend of GPP becomes more pronounced with the increase in CO_2 emissions from SSP1-2.6 to SSP5-8.5 scenarios. Under SSP1-2.6, the GPP shows a trend of first increasing and then decreasing, with a significant upward trend from 2014 to 2040, a slower growth rate from 2041 to 2020, and a decreasing trend from 2071 to 2100. Meanwhile, in other scenarios, there is an upward trend. Under SSP2-4.5, the growth trend is relatively obvious from 2014 to 2040 and 2041 to 2070, with a slowdown in growth from 2071 to 2100. In the other two scenarios, the growth trend of GPP is becoming larger and larger. (3) There are significant seasonal differences in the future changes of GPP in the Yangtze River Basin, with the greatest changes occurring in spring. Moreover, under the SSP2-4.5, SSP3-7.0, and SSP5-8.5 scenarios, the spring GPP may exceed the summer GPP, leading to an increased risk of future drought. The sub basins with large changes in GPP are concentrated in the Jialing River, Wujiang River, upper trunk stream, and Dongting Lake. The sub basins with small changes are the Jinsha River, Mintuo River, downstream main stream, and the Taihu Lake. The degree of change also increases with increasing CO_2 emissions under SSP1-2.6 to SSP5-8.5. (4) In general, the carbon sequestration capacity of the Yangtze River Basin will increase in the future, but

under the SSP1-2.6 scenario, it is necessary to guard against the risk of declining carbon sequestration capacity in the future. At the same time, the carbon sequestration capacity of Poyang Lake and Dongting Lake may decline in summer, while the large increase in the productivity of upstream vegetation needs to guard against the impact on downstream water resources in the future.

References

1. Chen, Y.; Gu, H.; Wang, M.; Gu, Q.; Ding, Z.; Ma, M.; Liu, R.; Tang, X. Contrasting Performance of the Remotely-Derived GPP Products over Different Climate Zones across China. *Remote Sens.* **2019**, *11*, 1855. [CrossRef]
2. Chen, Z.; Wang, W.; Fu, J. Vegetation response to precipitation anomalies under different climatic and biogeographical conditions in China. *Sci. Rep.* **2020**, *10*, 830. [CrossRef] [PubMed]
3. Anav, A.; Friedlingstein, P.; Beer, C.; Ciais, P.; Harper, A.; Jones, C.; Murray-Tortarolo, G.; Papale, D.; Parazoo, N.C.; Peylin, P.; et al. Spatiotemporal patterns of terrestrial gross primary production: A review. *Rev. Geophys.* **2015**, *53*, 785–818. [CrossRef]
4. Yu, G.; Zhu, X.; Fu, Y.; He, H.; Wang, Q.; Wen, X.; Li, X.; Zhang, L.; Zhang, L.; Su, W.; et al. Spatial patterns and climate drivers of carbon fluxes in terrestrial ecosystems of China. *Glob. Chang. Biol.* **2013**, *19*, 798–810. [CrossRef] [PubMed]
5. Hu, Z.; Wu, G.; Zhang, L.; Li, S.; Zhu, X.; Zheng, H.; Zhang, L.; Sun, X.; Yu, G. Modeling and partitioning of regional evapotranspiration using a Satellite-Driven Water-Carbon coupling model. *Remote Sens.* **2017**, *9*, 54. [CrossRef]
6. You, N.; Meng, J.; Zhu, L.; Jiang, S.; Zhu, L.; Li, F.; Kuo, L.J. Isolating the impacts of land Use/Cover change and climate change on the GPP in the heihe river basin of China. *J. Geophys. Res. Biogeosci.* **2020**, *125*, e2020JG005734. [CrossRef]
7. Sun, P.; Wu, Y.; Xiao, J.; Hui, J.; Hu, J.; Zhao, F.; Qiu, L.; Liu, S. Remote sensing and modeling fusion for investigating the ecosystem water-carbon coupling processes. *Sci. Total Environ.* **2019**, *697*, 134064. [CrossRef]
8. Ma, J.; Yan, X.; Dong, W.; Chou, J. Gross primary production of global forest ecosystems has been overestimated. *Sci. Rep.* **2015**, *5*, 10820. [CrossRef]
9. Aubinet, M.; Vesala, T.; Papale, D. *Eddy Covariance: A Practical Guide to Measurement and Data Analysis*; Springer Science & Business Media: Berlin, Germany, 2012.
10. Liu, S.M.; Xu, Z.W.; Wang, W.; Jia, Z.Z.; Zhu, M.J.; Bai, J.; Wang, J.M. A comparison of eddy-covariance and large aperture scintillometer measurements with respect to the energy balance closure problem. *Hydrol. Earth Syst. Sci.* **2011**, *15*, 1291–1306. [CrossRef]
11. Xie, X.; Li, A. An adjusted two-leaf light use efficiency model for improving GPP simulations over mountainous areas. *J. Geophys. Res. Atmos.* **2020**, *125*, e2019JD031702. [CrossRef]
12. Hu, Z.; Shi, H.; Cheng, K.; Wang, Y.P.; Piao, S.; Li, Y.; Zhang, L.; Xia, J.; Zhou, L.; Yuan, W. Joint structural and physiological control on the interannual variation in productivity in a temperate grassland: A data-model comparison. *Glob. Chang. Biol* **2018**, *24*, 2965–2979. [CrossRef]
13. Guan, X.; Chen, J.M.; Shen, H.; Xie, X. A modified two-leaf light use efficiency model for improving the simulation of GPP using a radiation scalar. *Agric. For. Meteorol.* **2021**, *307*, 108546. [CrossRef]
14. Marshall, M.; Tu, K.; Brown, J. Optimizing a remote sensing production efficiency model for macro-scale GPP and yield estimation in agroecosystems. *Remote Sens. Environ.* **2018**, *217*, 258–271. [CrossRef]
15. Anderson, M.C.; Norman, J.M.; Meyers, T.P.; Diak, G.R. An analytical model for estimating canopy transpiration and carbon assimilation fluxes based on canopy light-use efficiency. *Agric. For. Meteorol.* **2000**, *101*, 265–289. [CrossRef]
16. McCallum, I.; Franklin, O.; Moltchanova, E.; Merbold, L.; Schmullius, C.; Shvidenko, A.; Schepaschenko, D.; Fritz, S. Improved light and temperature responses for light-use-efficiency-based GPP models. *Biogeosciences* **2013**, *10*, 6577–6590. [CrossRef]
17. Potter, C.S.; Randerson, J.T.; Field, C.B.; Matson, P.A.; Vitousek, P.M.; Mooney, H.A.; Klooster, S.A. Terrestrial ecosystem production: A process model based on global satellite and surface data. *Glob. Biogeochem. Cycles* **1993**, *7*, 811–841. [CrossRef]

18. Prince, S.D.; Goward, S.N. Global primary production: A remote sensing approach. *J. Biogeogr.* **1995**, *22*, 815–835. [CrossRef]
19. Running, S.W.; Nemani, R.R.; Heinsch, F.A.; Zhao, M.; Reeves, M.; Hashimoto, H. A continuous satellite-derived measure of global terrestrial primary production. *Bioscience* **2004**, *54*, 547–560. [CrossRef]
20. Xiao, X.; Zhang, Q.; Braswell, B.; Urbanski, S.; Boles, S.; Wofsy, S.; Moore, B., III; Ojima, D. Modeling gross primary production of temperate deciduous broadleaf forest using satellite images and climate data. *Remote Sens. Environ.* **2004**, *91*, 256–270. [CrossRef]
21. Yuan, W.; Liu, S.; Zhou, G.; Zhou, G.; Tieszen, L.L.; Baldocchi, D.; Bernhofer, C.; Gholz, H.; Goldstein, A.H.; Goulden, M.L. Deriving a light use efficiency model from eddy covariance flux data for predicting daily gross primary production across biomes. *Agric. For. Meteorol.* **2007**, *143*, 189–207. [CrossRef]
22. Running, S.W.; Thornton, P.E.; Nemani, R.; Glassy, J.M. Global Terrestrial Gross and Net Primary Productivity from the Earth Observing System. In *Methods in Ecosystem Science*; Springer: New York, NY, USA, 2000; pp. 44–57.
23. Sjöström, M.; Ardö, J.; Arneth, A.; Boulain, N.; Cappelaere, B.; Eklundh, L.; De Grandcourt, A.; Kutsch, W.L.; Merbold, L.; Nouvellon, Y. Exploring the potential of MODIS EVI for modeling gross primary production across African ecosystems. *Remote Sens. Environ.* **2011**, *115*, 1081–1089. [CrossRef]
24. Huang, X.; Zheng, Y.; Zhang, H.; Lin, S.; Liang, S.; Li, X.; Ma, M.; Yuan, W. High spatial resolution vegetation gross primary production product: Algorithm and validation. *Sci. Remote Sens.* **2022**, *5*, 100049. [CrossRef]
25. Huntzinger, D.N.; Post, W.M.; Wei, Y.; Michalak, A.M.; West, T.O.; Jacobson, A.R.; Baker, I.T.; Chen, J.M.; Davis, K.J.; Hayes, D.J. North American Carbon Program (NACP) regional interim synthesis: Terrestrial biospheric model intercomparison. *Ecol. Model.* **2012**, *232*, 144–157. [CrossRef]
26. Yuan, W.; Liu, S.; Yu, G.; Bonnefond, J.; Chen, J.; Davis, K.; Desai, A.R.; Goldstein, A.H.; Gianelle, D.; Rossi, F. Global estimates of evapotranspiration and gross primary production based on MODIS and global meteorology data. *Remote Sens. Environ.* **2010**, *114*, 1416–1431. [CrossRef]
27. Wang, Z.; Liu, S.; Wang, Y.; Valbuena, R.; Wu, Y.; Kutia, M.; Zheng, Y.; Lu, W.; Zhu, Y.; Zhao, M.; et al. Tighten the bolts and nuts on GPP estimations from sites to the globe: An assessment of remote sensing based LUE models and supporting data fields. *Remote Sens.* **2021**, *13*, 168. [CrossRef]
28. Yuan, W.; Cai, W.; Xia, J.; Chen, J.; Liu, S.; Dong, W.; Merbold, L.; Law, B.; Arain, A.; Beringer, J.; et al. Global comparison of light use efficiency models for simulating terrestrial vegetation gross primary production based on the LaThuile database. *Agric. For. Meteorol.* **2014**, *192–193*, 108–120. [CrossRef]
29. Chen, Y.; Feng, X.; Fu, B.; Wu, X.; Gao, Z. Improved global maps of the optimum growth temperature, maximum light use efficiency, and gross primary production for vegetation. *J. Geophys. Res. Biogeosci.* **2021**, *126*, e2020JG005651. [CrossRef]
30. He, J.; Yang, K.; Tang, W.; Lu, H.; Qin, J.; Chen, Y.; Li, X. The first high-resolution meteorological forcing dataset for land process studies over China. *Sci. Data* **2020**, *7*, 25. [CrossRef]
31. Cheng, W.; Dan, L.; Deng, X.; Feng, J.; Wang, Y.; Peng, J.; Tian, J.; Qi, W.; Liu, Z.; Zheng, X. Global monthly gridded atmospheric carbon dioxide concentrations under the historical and future scenarios. *Sci. Data* **2022**, *9*, 83. [CrossRef]
32. Ge, W.; Deng, L.; Wang, F.; Han, J. Quantifying the contributions of human activities and climate change to vegetation net primary productivity dynamics in China from 2001 to 2016. *Sci. Total Environ.* **2021**, *773*, 145648. [CrossRef]
33. Piao, S.; Yin, G.; Tan, J.; Cheng, L.; Huang, M.; Li, Y.; Liu, R.; Mao, J.; Myneni, R.B.; Peng, S.; et al. Detection and attribution of vegetation greening trend in China over the last 30 years. *Glob. Chang. Biol* **2015**, *21*, 1601–1609. [CrossRef] [PubMed]
34. Piao, S.; Wang, X.; Park, T.; Chen, C.; Lian, X.; He, Y.; Bjerke, J.W.; Chen, A.; Ciais, P.; Tømmervik, H.; et al. Characteristics, drivers and feedbacks of global greening. *Nat. Rev. Earth Environ.* **2019**, *1*, 14–27. [CrossRef]
35. Zhu, Z.; Piao, S.; Myneni, R.B.; Huang, M.; Zeng, Z.; Canadell, J.G.; Ciais, P.; Sitch, S.; Friedlingstein, P.; Arneth, A.; et al. Greening of the Earth and its drivers. *Nat. Clim. Chang.* **2016**, *6*, 791–795. [CrossRef]
36. Keenan, T.F.; Hollinger, D.Y.; Bohrer, G.; Dragoni, D.; Munger, J.W.; Schmid, H.P.; Richardson, A.D. Increase in forest water-use efficiency as atmospheric carbon dioxide concentrations rise. *Nature* **2013**, *499*, 324–327. [CrossRef] [PubMed]
37. Fensholt, R.; Langanke, T.; Rasmussen, K.; Reenberg, A.; Prince, S.D.; Tucker, C.; Scholes, R.J.; Le, Q.B.; Bondeau, A.; Eastman, R.; et al. Greenness in semi-arid areas across the globe 1981–2007—An Earth Observing Satellite based analysis of trends and drivers. *Remote Sens. Environ.* **2012**, *121*, 144–158. [CrossRef]
38. He, P.; Ma, X.; Meng, X.; Han, Z.; Liu, H.; Sun, Z. Spatiotemporal evolutionary and mechanism analysis of grassland GPP in China. *Ecol. Indic.* **2022**, *143*, 109323. [CrossRef]
39. Xu, L.; Myneni, R.B.; Chapin, F.S., III; Callaghan, T.V.; Pinzon, J.E.; Tucker, C.J.; Zhu, Z.; Bi, J.; Ciais, P.; Tømmervik, H.; et al. Temperature and vegetation seasonality diminishment over northern lands. *Nat. Clim. Chang.* **2013**, *3*, 581–586. [CrossRef]
40. Chakraborty, T.; Lee, X.; Lawrence, D.M. Diffuse Radiation Forcing Constraints on Gross Primary Productivity and Global Terrestrial Evapotranspiration. *Earth's Future* **2022**, *10*, e2022EF002805. [CrossRef]
41. Ezhova, E.; Ylivinkka, I.; Kuusk, J.; Komsaare, K.; Vana, M.; Krasnova, A.; Noe, S.; Arshinov, M.; Belan, B.; Park, S.-B.; et al. Direct effect of aerosols on solar radiation and gross primary production in boreal and hemiboreal forests. *Atmos. Chem. Phys.* **2018**, *18*, 17863–17881. [CrossRef]
42. Cernusak, L.A.; Haverd, V.; Brendel, O.; Le Thiec, D.; Guehl, J.; Cuntz, M. Robust response of terrestrial plants to rising CO_2. *Trends Plant Sci.* **2019**, *24*, 578–586. [CrossRef]
43. Swann, A.L.S.; Hoffman, F.M.; Koven, C.D.; Randerson, J.T. Plant responses to increasing CO_2 reduce estimates of climate impacts on drought severity. *Proc. Natl. Acad. Sci. USA* **2016**, *113*, 10019–10024. [CrossRef] [PubMed]

44. Richardson, A.D.; Andy Black, T.; Ciais, P.; Delbart, N.; Friedl, M.A.; Gobron, N.; Hollinger, D.Y.; Kutsch, W.L.; Longdoz, B.; Luyssaert, S. Influence of spring and autumn phenological transitions on forest ecosystem productivity. *Philos. Trans. R. Soc. B Biol. Sci.* **2010**, *365*, 3227–3246. [CrossRef] [PubMed]

45. Medlyn, B.E.; Dreyer, E.; Ellsworth, D.; Forstreuter, M.; Harley, P.C.; Kirschbaum, M.; Le Roux, X.; Montpied, P.; Strassemeyer, J.; Walcroft, A. Temperature response of parameters of a biochemically based model of photosynthesis. II. A review of experimental data. *Plant Cell Environ.* **2002**, *25*, 1167–1179. [CrossRef]

46. Gan, G.; Liu, Y.; Sun, G. Understanding interactions among climate, water, and vegetation with the Budyko framework. *Earth-Sci. Rev.* **2021**, *212*, 103451. [CrossRef]

47. Winkler, A.J.; Myneni, R.B.; Hannart, A.; Sitch, S.; Haverd, V.; Lombardozzi, D.; Arora, V.K.; Pongratz, J.; Nabel, J.E.M.S.; Goll, D.S.; et al. Slowdown of the greening trend in natural vegetation with further rise in atmospheric CO_2. *Biogeosciences* **2021**, *18*, 4985–5010. [CrossRef]

48. Wang, S.; Zhang, Y.; Ju, W.; Chen, J.M.; Ciais, P.; Cescatti, A.; Sardans, J.; Janssens, I.A.; Wu, M.; Berry, J.A. Recent global decline of CO2 fertilization effects on vegetation photosynthesis. *Science* **2020**, *370*, 1295–1300. [CrossRef]